JOURNAL OF CONDENSED MATTER NUCLEAR SCIENCE

Experiments and Methods in Cold Fusion

13th International Workshop on Anomalies in Hydrogen Loaded Metals, Oasi di Greccio (Lazio, Italy), 5–9 October 2018

VOLUME 30, January 2020

JOURNAL OF CONDENSED MATTER NUCLEAR SCIENCE

Experiments and Methods in Cold Fusion

JOURNAL OF CONDENSED MATTER NUCLEAR SCIENCE

Volume 30, January 2020

ISSN 2227-3123

Orders, claims, author inquiries and journal inquiries

Please contact the Editor in Chief, CMNSEditor@iscmns.org or webmaster@iscmns.org

J. Condensed Matter Nucl. Sci. 30 (2020) 1–65
 ISSN 2227-3123

JOURNAL OF CONDENSED MATTER NUCLEAR SCIENCE

Volume 30 2020

CONTENTS

RESEARCH ARTICLES

Preface

The 13th International Workshop on Anomalies in Hydrogen Loaded Metals was held in the Oasi di Greccio (Lazio, Italy)

The 13th International Workshop on Anomalies in Hydrogen Loaded Metals was held in the Oasi di Greccio (Lazio, Italy) at an altitude of 700 m set in beautiful woodland on the mountainside. Despite being held only four months after ICCF21 in Colorado, the Workshop was well attended with 43 participants. Further details can be found at http://iscmns.org/work13/.

This was the first ISCMNS workshop co-chaired by Claudio Pace and we owe him our thanks for arranging such good value for money and local organization. Although no financial subsidies were received, the cost for four nights including board and lodging was kept down to EUR 600. Early registrants paid only EUR 500.

The Oasi di Greccio in keeping with previous policy is a self-contained conference center and making the conference fee "all inclusive" encouraged participants to stay in the building. So did the open bar in the foyer!

An excursion was organized to the Marmore waterfalls and the Banquet was held at the Nido del Corvo restaurant in Greccio.

Sincerely,

Dr. Bill Collis
(*Chair*)
January 2020

J. Condensed Matter Nucl. Sci. 30 (2020) 1–24

Research Article

Nuclear Structure and Cold Fusion

John P. Wallace*
Casting Analysis Corp., 8379 Ursa Lane, Weyers Cave, Virginia 24486, USA

Michael J. Wallace
Phoenix, AZ 85050, USA

Abstract

Combining advances in understanding the strong force with experiments on lattice fusion allows a description of lattice D–D fusion to be constructed. What has to be exposed is a nuclear energy loss mechanism leaving little or no residual radioactivity. The requirements on the lattice for D–D fusion are strict and appear to be limited to particular FCC lattices within a range of lattice parameters. A mechanical understanding is needed of how elevated local concentrations of deuterium are achieved while avoiding being trapped at defect sites. Using optical, RF, and experimental anomalous heat data the metallurgical requirements for the process is refined by considering a combination of diffusion, partial molar volume, positron annihilation data, defect kinetics, and electronic band structure allowing logical exhaustion to identify the kinetic structure that drives lattice nuclear fusion.
 ISSN 2227-3123

Keywords: Cold fusion, Deuterium, Lattice, Metallurgy, Nuclear structure, Quantum mechanics

1. Introduction

In physics there are not many landmark experiments that use absolute measurements. Joule's conservation of mechanical and thermal energy, the Compton scattering experiment, the radiationless electron scattering ionization of the hydrogen 1S state [1], and now cold fusion experiments producing transmutations at thermal energies. Most experiments are done with differential measurements comparing two similar states where there has been a transition either atomic or nuclear. Such simple comparisons shields the experimenter from the responsibility of having an accurate description of the state's structure because of the differential nature of the measurement. Lattice cold fusion cannot be treated by such a simple approach.

Lattice cold fusion that is initiated by gas phase charging has the lowest input energy of all the non high energy methods that drive transmutation. This particular process represents the minimum in material and energy overhead required to drive a nuclear reaction. It is this very economic process that needs to be understood.

*E-mail: jpw@castinganalysis.com.

 ISSN 2227-3123

The advantage in studying cold lattice nuclear processes is that a window opens on a number of poorly understood areas: solid state interstitial behavior, nuclear structures [2], crustal transmutations [3], dust fusion [4], and the role of condensed plasmoids [5]. By beginning with the behavior of the hydrogen isotopes on the interstitial FCC lattice initiating a nuclear process at thermal energies sets the minimum conditions for the fusion process. The physics supported by these transmutation processes openly questions the validity of a number of models about nuclear structure, the earths crustal chemistry, standard solar model, along with the current dogma that claims the electron neutrino possess mass [6,7]. The reward in making a mistake on such a basic physical process as fusion is to have all that was built without its use brought into question.

The prime difficulty in understanding the conditions for D–D fusion in the solid state is that scale properties from lab dimensions down to nuclear scale all come into play. To explain the process a path has to be constructed through these descending scales. If a mechanism for D–D fusion can be defended then the slightly higher energy mechanisms that alter the heavier element distribution by both fission and fusion in the earth's crust and space can be more easily approached.

2. Crystal Structure and Lattice Parameter

Successful experiments supporting cold fusion that have had their details published appear to have a common thread: a favored crystal structure and a narrow range of lattice parameters supporting the process. Latticed parameter can be affected in three ways, damage induced strains, [8], alloying [9,10], high thermal gradients [11], and by a combination of these methods. By alloying, the lattice parameter can be adjusted in three ways, alloy to a single composition, have a concentration gradient by diffusion between two metals, i.e. Cu–Ni or mechanical alloying at an interface, example Ni–Pd. When alloyed to single composition a strong thermal gradient seems to be required for having active sites as heat is produced and the internal temperature gradient alters the lattice parameter locally.

Our focus will be on cold fusion experiments reported for palladium, nickel, their alloys, and nickel–copper alloys, Table 1. Titanium would be the odd metal in this group as it is crystal structure is HCP and not FCC. However, with a stacking fault generated in deformation, there are FCC transformed local regions in deformed titanium.

Popular theories for describing lattice enhanced fusion tend to stress increases in lattice volumes due to vacancies in super abundance [12] and other large defects such as microcracks [13]. Neither model supplies a compact confinement structure required for fusion, but rather supplies excess volume. This excess volume comes from vacancies created during the deuterium charging process where the metal is damaged as a precursor for microvoid formation, which is necessary step in collecting then discharging the light ions into a supersaturated lattice on microvoid collapse. From the initial experiments of Fleischmann and Pons the damage and metallurgical recovery process has been part of the cold fusion prescription. Recovery via microvoid formation and collapse has been studied by positron annihilation [14,15], however, it has never been fully explained in detail. The creation of vacancies, their collection into microvoids, hydrogen isotopes being captured in the microvoids, and the microvoid collapse are all essential features of the damage driven D–D lattice cold fusion process, but are only the preliminary steps to the final fusion. It was shown studying hydrogen behavior in iron that only when hydrogen has been purged from the material, does the positron long life time component vanish, which had been long associated with the presence of microvoids [16]. A clean internal microvoid not coated with hydrogen or deuterium presents no barrier for the conversion of a trapped triplet positronium, the long lived species, $\sim$1000 ps, to singlet positron that promptly decays with a short lifetime, $\sim$100 ps. The measured long life times in damaged metals appear not to be a signature of the presence of microvoids, but microvoids with internal surface contamination that can preserve the triplet state of positronium. The principal contaminants found in microvoids are the fast diffusing hydrogen isotopes.

Recently it appears that the requirement to do damage prior to charging in monolithic metal host may have been overcome by Mizuno in a process of mechanical alloying where he transferred palladium to a fine nickel screen by

Table 1. Even though the coefficient of thermal lattice expansion differs by $\sim$10% between palladium and nickel based on their lattice parameters the difference is only only 0.3% which in part explains the complete solid solution over their entire range of temperature and composition. This coupled with their matched mechanical elastic modulus sets up the condition that grain boundaries might not be highly favored interface structure at a nickel–palladium interface allowing the boundary to reconstruct with the composition change occurring over a few unit cells. The other unique feature for the pair of metals is the peak in electron density at the Fermi surface compared to other metals allowing enhanced ion screening [31].

Element	Lattice Parameter	$\frac{m}{m^{\circ}\mathrm{K}}$	Bulk Mod. GPas.	e^- state density
Cu	3.597	16.7	123	.3
Ni	3.5168	13.0	180	4.8
Pd	3.8827	11.8	180	3.2

rubbing [10]. This process of mechanical alloying solved two long standing problems. One to provide easy entry of hydrogen to a reaction zone via the palladium free surface, while creating an array of interstitial sites with varying volumes from what is found in undamaged nickel to that of undamaged palladium. These will be distributed through the interface of the two metals and constitute the result of mechanical alloying. It is not only a particular interstitial volume that will be important as an active site it is also having other sites with slightly different volumes active as temperature changes. This range of sites must exist in quantity.

2.1. Unique metallurgical site

There are a number of lattice assisted cold fusion experiments reported for palladium, nickel, their alloys, nickel-copper alloys and titanium. The hydrides and deformed regions of these metals, which are generated on hydrogen isotope charging, are of less interest in the final act of driving a fusion process because they represent regions of increased volume that can trap and isolate the hydrogen isotopes as atomic species with a bound electron. This is evident in the atomic transitions of the triplet to singlet atomic deuterium transition at 327 MHz in the recent experiments by Swartz [17]. What is required to drive fusion is a strong, compact, symmetric, and constrained cavity. The deformation pathway to cold fusion needs three precursors: first to generate vacancies that form microvoids for collecting hydrogen isotopes that can then be discharged on collapse. Second is to introduce damaged regions in the crystal as a whole, putting the undamaged FCC regions in a state of increased tension for nickel and compression for palladium, and third to increase the anharmonic potentials between the undamaged FCC regions and the damaged volumes.

The metals have to be viewed as a mixture of undamaged and damaged portions some of which maybe hydrides. This overall damage is driven by the large partial molar volumes of the hydrogen isotopes [18] facilitating the occupancy of the interstitial octahedral sites with a pair of deuterium ions. Two deuterium occupying a single site is favored over two protons because of the smaller dynamic volume of the deuterium ion on the tightly constrained interstitial site due to deuterium's greater mass.

The FCC structure is of interest because of its high symmetry both on the atom site, but also on the highly

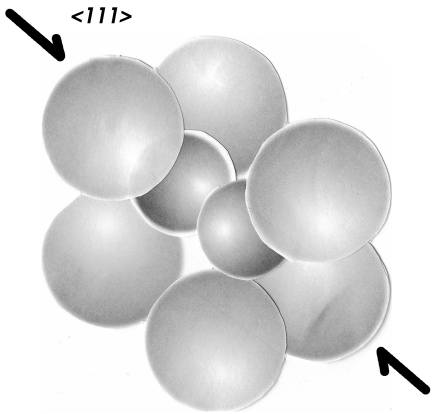

Figure 1. Two deuterium ions oriented along a $\langle 111 \rangle$ axis in the FCC octahedral interstitial site. Even though this same geometry of eight elements can be reproduced in the HCP lattice the cubic symmetry of the restraint provided by the rest of the lattice is lost along the three remaining equivalent orientations of the FCC site.

symmetric regular octahedral interstitial site. This combination is unique and not found in any other metal crystal systems. All other interstitial sites are irregular and of lower symmetry. The FCC octahedral site is a large site compared to other FCC and BCC interstitial sites and with six metal atoms coordination forms a cage capable of packing two interstitial D ions and holding them together in close proximity, Fig. 1. The FCC lattice unlike the diamond cubic lattice is a densely packed cubic structure. The utility of the FCC lattice's octahedral site for cold fusion is that it can act as a closed die forge where there are 4 independent $\langle 111 \rangle$ axis available for constraining two D ions making their capture much easier and escape more difficult. Each deuterium ion is cradled by three metal atoms minimizing the D ion from slipping laterally. If it does slip it will be captured by another three metal atom barrier of the site. This is where the four independent $\langle 111 \rangle$ axis along which D–D contact is constrained, eliminates an easy escape from the closed die forge the site creates. Just as important is the symmetric coordination of the supporting metal atom, that is 12 in the FCC, and this symmetry is lost in the HCP and BCC lattice. The coordination of six for the octahedral FCC interstitial site is high for an interstitial site, but the necessary minimum to support two trapped ions per site. The BCC octahedral site is not symmetric and squashed along the cube axis. Neither micro-cracks nor super abundant vacancies provide the constraints to bring two D ions in close proximity as does the FCC octahedral interstitial site to drive fusion.

The atom site or vacancy site on the FCC lattice has 12 nearest neighbor coordination, however, the central site sees six cube faces on the three principal cube axis. The cube face does not provide the same constraint for compression as the interstitial faces which are composed of three nearest neighbors.

Two different experiments were key in drawing our attention to the high symmetry sites in the lattice as being critical to drive nuclear activity. These experiments were the Raman measurements of Stokes/anti-Stokes lines [19,20] and the dual laser beating [13], that in both cases are sampling the energetic optical phonon. There are two high symmetry points in the FCC lattice: the atom site and the median edge site that is also the location of the interstitial octahedral site.

2.2. Anharmonic compression

Fusion is inhibited by electrostatic repulsion of ions and can be reduced by dynamic screening, however, an additional mechanism is required to drive the ions together. In the deuterium charged lattice there are regions of hydride formation and significant damage and regions of undamaged FCC lattice with interstitial deuterium. This composite material will lose its normal low amplitude linear elastic properties as the anharmonic terms can grow with the increased concentration of deuterium on the interstitial lattice. It has also been pointed out that fusion will be assisted in anharmonic regions by the periodic localization of high intensity lattice vibrations first studied by Fermi, Pasta and Ulam and recently being considered as a way to enhance catalysis, both chemical and nuclear [21]. For this mating process to drive fusion a compact lattice structure is needed to push the two ions together along with a dynamic screening process to suppress the repulsion.

2.3. Interstitial sites metallurgy

One of the most powerful tools in understanding interstitial behavior in metals are the activation energies for diffusion. If they are large then the diffusion process can be treated in the tradition classical way of using a configuration energy barrier which must be overcome. However, the activation energies fall into the range ~ 0.1 eV or less then the classical model fails. For the light interstitial such as the hydrogen isotopes imaging them is not possible. One nice feature of the activation energy of diffusion measurements is that the fast diffusion processes are not masked as the slower process can be masked. The most extensively studied couple is H–Fe where hydrogen is a very rapidly diffusing species with an activation energy of 0.047 eV, where there are a number of failure mechanisms in which hydrogen participates. There is a large mass effect for deuterium whose activation energy is 0.082 eV in iron. These small activation energies are dictated by two characteristics, first the light isotopes are in a very compact site and cannot be screened, they are naked ions. They behave as bare charges and strongly perturb their sites expanding them that is revealed in their significant measured partial molar volumes. The second feature affecting the activation energy is the potential well depth, which can be computed from a quantum model that is consistent with the activation energies of the three hydrogen isotopes [22].

The metallurgy of the hydrogen isotopes in the FCC metals is more complex because of the large site size for a single interstitial occupant. The advantage for fusion in the FCC metal are the interstitial potential wells are not that shallow allowing a high energy non-equilibrium configuration of interstitial pairs. Nickel and palladium share three characteristic that are important relative to the behavior of the interstitial isotopes of hydrogen. The hydrogen interstitial sites for nickel and palladium are rather deep and have nearly the same activation energy for diffusion. Indicating their sites are rather similar even though their lattice parameters differ. The highly symmetric location for the principal octahedral interstitial site and the high symmetry of the site itself in FCC metals makes it a more flexible site to abuse without destruction by the addition of a second interstitial. There is no preferred orientation for a distortion as would be the case for a lower symmetry site. In the BCC lattice the interstitial sites do not have a high symmetry that leads to axial distortions and instability with a single interstitial and collectively leads to problems of embrittlement, blistering, and attack found in iron and niobium [23].

The macroscopic laboratory scale comes into play when trying to determine where in a metal lattice such process should occur. One can force the lattice parameter of a material to lower values through hydro-static compression, however, the same is not easily accomplished in expanding the lattice. It is easier to expand the lattice nearer to a free surface and this is where damage caused by hydrogen or deuterium charging is predominately found, within a micron of the surface and where cold fusion was traced by transmutation products [24].

Table 2. Metallurgical preliminaries required for damage controlled cold fusion.

Substrate
Solid state process not liquid state at 1 atm.
FCC not BCC
Ni & Pd band structure
^{2}H Mass favorable for interstitial binding
Loading → Slow
High gradient strain fields from ^{2}H loading
Dislocation formation and flow
Vacancy generation
New phases
Microvoid formation
Recovery → More rapid
Near surface strain relaxation gradients
Vacancy trapping of ^{2}H
Vacancy diffusion to free surfaces
Microvoid enrichment with ^{2}H
Microvoid collapse → Fast
Charge stripping of ^{2}H from collapse
Inject the lattice with high interstitial conc.
Double site occupancy
Local current for dynamic screening
D–D fusion

2.4. Damage mediated cold fusion and dynamic recovery

Electro-chemical, plasma, or vapor phase charging of either nickel or palladium with deuterium drives the alloying of the metal with hydrogen isotopes. It is difficult to describe this process as a simple steady state process because the state of stress in the disturbed volume varies continuously going into the material leaving a wake of damage that affects both the diffusion front and the stress state within the metal. This process does not move as a simple plane front, but produces both islands of damaged material in an undamaged matrix, analogous to a two phase mixture. The ability of strained sites to expand changes as both a function of depth and damage. The problem is damage is continually induced into the metal, which will try to recover via different pathways [25]. The near surface has a major effect on the damage profile and the local strains achieved in the lattice, Table 2.

The question that is necessary to ask is how can a lattice be primed with a high concentration of non-trapped interstitial deuterium that will produce a small population of di-deuterium interstitial? Two dynamic processes are required. One is to remove the population of free trapping sites for deuterium while also dumping a quantity of free unscreened interstitial deuterium onto the interstitial lattice. This is essential in order to get sufficient concentration so that two deuterium can for a short time share the same interstitial location.

Nano-structures are helpful because of the large surface area with a reduced strain energy for expanding an interstitial site near a free surface. The process of recovery is one where vacancies generated by the strain induce charging damage diffuse and collect into microvoids. These microvoids will eventually collapse and generate prismatic dislocation loops as a signature of their former existence. Positron annihilation lifetime measurement of the long lifetime component and its intensity can also be used to study microvoids, because the long lifetime component is found in deformed metals with both FCC and BCC structures [15]. However, the interpretation of the data requires some care.

A common way is to take a the long lifetime component as a measure of multiple vacancies in a clusters. The argument of Sakai that the long lifetime component is proportional to size of the vacancy cluster is flawed, because within a microvoid with more than a few vacancies positronium can form in either of two states: triplet or singlet. The singlet state has a very rapid decay on the order of 100 ps The triplet state more than 1000 ps. In a microvoid where the interior surfaces are clean, meaning not covered by a monolayer of adsorbed interstitial, then the conversion of triplet to singlet state should be quite rapid and there should be no long lifetime component. This was confirmed in deformed iron that had been purged of hydrogen [16], where the long lifetime component vanished.

Purging hydrogen from metals is not a simple process requiring vacuum melting and long high temperature anneals in a hydrogen free atmosphere with external hydrogen getters. Normally in deformed metals containing trace hydrogen there is a strong long lifetime component in deformed and recovered specimens. Dynamic recovery when microvoids are generated sees their population drop on recovery. If these microvoid interior surfaces are covered with hydrogen, then this hydrogen will be dumped into the latticed on the microvoid's collapse creating a local super saturation on the interstitial lattice. A local super saturation of deuterium will supply ions to doubly occupy the FCC octahedral sites and precipitate a nuclear fusion. Unfortunately, the penetration depth of positrons is on the order of 10s of microns, greater than the 1 micron depth found for transmutations, which limits its utility as a near surface probe for damage [24].

3. Dynamic Screening

Complicating atomic, solid state, and nuclear physics is the failure in standard quantum mechanics to develop structural information about electron and nuclear structures, which has inconveniently left the analysis of cold fusion in limbo. Quantum mechanics is an incomplete subject poorly treated by mathematicians who forced the subject into forms they are familiar with. Because of a failure to strictly conserve total energy during its development from 1927 to 1934, relativity was not properly treated. The first of these mistakes was taking the form of the Dirac equation as being good relativistic description for the electron. This is evident because it fails to generate a physical ground state for the 1S hydrogen atom [26] principally because it is a linear approximation of a second order equation. Dirac in 1932 tried to back away from this method but failed to find an alternative method [27]. This left a legacy that relativity in quantum mechanics could be treated with a first order equation. Following WWII there was a race to find the corrections to non-relativistic Schrödinger equation solution for atomic hydrogen, which also was an approximation. The experimental advances made by Kusch [28] and Lamb [29] was in part to provide information not only about atomic properties but also nuclear properties. The nuclear contributions were completely ignored by the race to produce quantum electrodynamics. Small corrections to a damaged theory of non-relativistic quantum mechanics does not ensure a correct theory particularly if non-unique methods were employed. Starting with these mistakes, high and low energy quantum theories diverged to increase the confusion over the years. What was lost was a structural description of fields and matter. This can now be treated with differential equations that describe quantum structure derived directly from the relativistic energy conservation relations [30,2].

To understand dynamic screening by the lattice electron of two closely confined positive ions requires knowledge of the electron's charge structure. The electron structure comes directly from its field structure and its charge density is plotted in Fig. 2 [1]. The scale of the electron's charge density determines the scale of minimum approach of two ions without supplying additional energy, when screened by the dynamics of the lattice electrons. Attempts have been made to explain dynamic screening by a compact electronic structure by using fractional quantum states from the Schrödinger equation and deep lying states via the Dirac equation. These approaches fail in two ways: the deep states have never been detected in scattering experiments and the approaches fail to produce structural information about the electron.

Palladium and nickel are unique among the metals in the structure of their available valence electron density of

state just at the fermi surface, showing a very large density of available electrons that can be activated with a minimum of energy to provide dynamic screening currents between the positive ions, Table 1 [31]. This near singularity in density of states enhancement approaching the fermi surface is not found in any other FCC or BCC metals.

Screening as computed from density function theory is handled as a static polarization of the valence electrons including the exchange and correlation effects that works well at low density metals or at low density molecular orbital. However, in the compact region of the interstitial sites that deuterium occupies, the small scale structures cannot be screened by this quasi-static mechanism where density function theory fails at its lower bound [22]. An alternative mechanism for screening the two ions is required. A process to dynamically screen a free charge is available in nickel and palladium, because of the unique band structure in nickel, palladium, and their alloys with a high density of states at the fermi surface permits currents to be generated from the minimal electrostatic attraction of the deuterium ions. This characteristic band structure is also the source of the catalytic abilities found for these two metals. The location of the octahedral site on a cube edge allows 6 separate currents to be generated while maintaining overall charge neutrality. The cubic symmetry of the site allows for this multiplicity of current to dynamically screen two deuterium ions and drawing them together in any of their four possible orientations on the octahedral site, Fig. 3. The limits to screening is controlled by the structural dimension of the electron charge distribution. The electron has a structural charge radius on the order of $\hbar/mc \sim 4 \times 10^{-13}$ m which now becomes the minimum scale where complete screening can occur [1]. The process of dynamics screening can take on a second role when the ions are close and energy is being shed to the electrons as nuclear binding progresses. This second role is the removal of energy via a potential interaction with the altered nucleon charge density distribution. Such direct interactions have been postulated to provide a means of incrementally removing the mass defect energy from the nucleus and dumping it into the lattice via electron scattering to an increased phonon population [32]. Recent accelerator experimental data have found a positive result in the study of H–D fusion in a solid target where the energy removed in less than 10% of the reactions was by an electron [33]. This was not weak decay process but a prompt lattice electron that was ejected with the excess characteristic fusion energy.

4. Nuclear Structure

Having found a way to get two nuclei in close proximity it is now necessary to understand how the strong force functions to produce a fusion reaction. Fusion even in the core of the sun at its elevated pressure and temperature is not a common phenomenon. It is only the sheer volume of the sun that allows it to produce sufficient heat to bring its surface temperature to ∼5700°C. To study cold fusion knowledge of the strong force is essential. There are few scattering experiments that produce unambiguous information about the strong force. One of these experiments will be used to test a model of the strong force so it can be used with confidence in describing fusion. In accelerator experiment to drive D–D fusion there is no lower bound cut off found experimentally for this process down to the 10 keV range and that might indicate that at low energies polarization of the approaching nucleons are affected not only by electrostatic polarization to reduce the interaction barrier but also strong force polarization of the deuterium.

To excise the concept of a point charge in nuclear structure requires a look at the late 19th century attempt by mathematicians to perfect analysis, the calculus. The idea that the mathematical continuum does not represent a physical space where quantum mechanics can be produced was never seriously considered during the 1930s. The quickest way to understand the importance of this omission is based on a two part argument taken from the work of Georg Cantor the 19th century mathematician concerned with the orders of infinity [34]. Cantor proved a series of theorems about the mathematical continuum and one of these theorems stated that with a continuum defined space, dimensions become only a labeling scheme [35]. Dimensions are not a unique or necessary features of the continuum's mathematical landscape other than as a flexible accounting mechanism. The indexes defining the dimensions can be rearranged at will and are not uniquely associated with a particular dimensional structure of space. Physically, there is

considerable experimental evidence that spatial dimensions are real, definable, and a necessary delineation for defining a physical space. Particularly, for defining the properties of the one and two dimensional components of the baryons, the quarks. Dimensions are the major component in defining a quantized charge and the structure of matter and are not an arbitrary convenience. The inescapable logical deduction is that a physical space cannot be represented by the continuum, and must be replaced with a less compact description where dimensions have physical meaning.

To be consistent with relativity and the conservation of energy, two spaces are required, one to define the self-energy of an individual particle or a field, named the self-reference frame, and the second space is the normal laboratory frame for dynamics where measurements are made. These spaces are statistically independent, bring in the probabilities of quantum mechanics. With this change, the point mass and point charge of classical physics are lost [2,30].

The observer [36,37] is not an essential part of the measurement for the particles and fields because they are individually subject to comparisons by their dual descriptions in both the self-reference frame and laboratory frame. The two complementing frames of reference are statistically independent, eliminates the need for an observer. The comparison captures the limitation on the scales that can be used in describing physical behavior and concurrently defines the limitation of their space. This same mechanism can then be used to describe higher level emergent processes. The structure of the electron is of importance in that its scale and charge distribution define the lower limit of where dynamic screening becomes ineffective.

In this new view of quantum mechanics potential generated forces have their origin in the structure of the particles themselves. For these potential generated forces there is no need to invent an exchange boson to carry the force. These potential generated forces are essentially contact interactions over a volume. This removed the difficulty in explaining the origin of the electrostatic interaction.

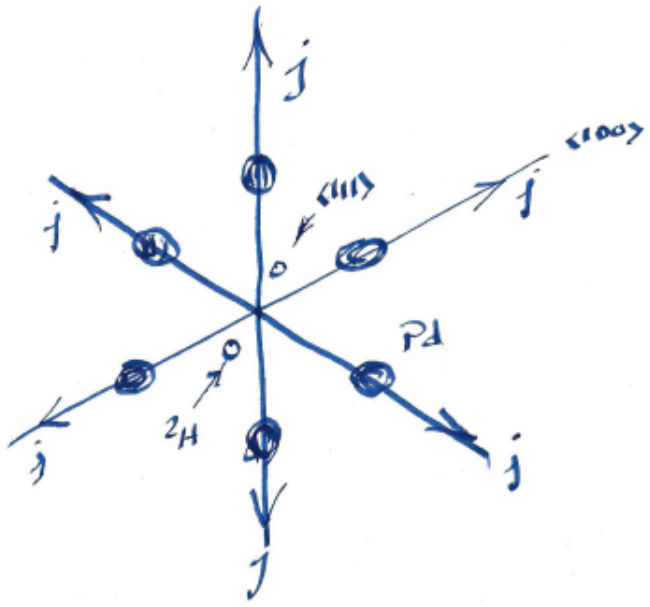

Figure 2. The electronic currents, *j*, along the cube axis dynamically screen the deuterium ion pair centered on the octahedral interstitial site.

4.1. Nucleons

Experiment has revealed the protons and neutrons are composite particles constructed of fractionally charged components. Nucleon structures were not revealed in those experiments. These components can be constructed from the lower dimensional massive solutions found in the self-reference frame [30]. These solutions in product combination generate the particle structure. Yet the components are not individually isolated from each other as was originally thought from the early electron-scattering parton experiments [38]. The early nuclear model was complex. A family of fields was postulated in the early 1960s called gluon to hold the components together by their exchange [39]. Though none have ever been detected, they were assumed to exist because of three jet decays found in high energy collisions. This was not a direct observation of the gluon and thus a very tenuous explanation. The gluon picture of nuclear structure will not be used. Recent high energy experiments now support a structural description of the baryons. Deuterium's ground state which is the simplest bound state of two baryons can be modeled by only considering the overlap in the two nuclei state functions. A second high energy form of deuterium can also be modeled, which occurs when the proton is driven into the neutron during a short range correlation by a high energy electron [40]. This state can be modeled by just using the product state of the six lower dimensional quark components [2].

Using the description of the two lower dimension fermion fields, 1D and 2D, as defined in the self-reference frame to represent the up and down quark. What is meant by lower dimensional components are not Euclidean lines and planes rather functions where volume is defined as $V \sim a^n$ where *a* is a scale and *n* is the dimension. These fields can be found as the spatial solutions from equation 1 which is derived from the relativistic conservation relation for the dimension $n = 1$ and 2, κ is proportional to mass and is one over the particle's scale ϵ, and γ is from relativity scaling the relative motion [2].

$$\frac{\partial^2 \mathbf{u}(r)}{\partial r^2} + \left(\frac{n-1}{r} + \kappa\{1 - i\gamma\} \right) \frac{\partial \mathbf{u}(r)}{\partial r} - i\kappa^2 \gamma \mathbf{u}(r) = 0. \tag{1}$$

This equation generates solutions for both fermions and bosons in the particles self-reference frame, where ${}_1F_1$ and U are the confluent hypergeometric functions for the case when $\gamma = 1$, relative rest, that respectively represents fermion and boson wave function.

$$\begin{aligned} \mathbf{u}^{\mathrm{f}}(r,n) &= \mathrm{e}^{-\kappa r}{}_1F_1\left[\frac{n-1}{1+i}, n-1, (1+i)\kappa r \right], \\ \mathbf{u}^{\mathrm{b}}(r,n) &= \mathrm{e}^{-\kappa r} U\left[\frac{n-1}{1+i}, n-1, (1+i)\kappa r \right]. \end{aligned} \tag{2}$$

To construct the proton's strong force structure a product of the lower dimension solutions will be used and their scale ratios determine the mass, $m \sim= (\kappa_1 + \kappa_2 + \kappa_3)\hbar/c$. Similar to Eq. (1) there is a differential equation for the massless fields, Eq. (4), in the self-reference frame and it will be used to extract the lower dimension boson solutions [2], Table 3.

Total charge of a fermion particle is a mass independent quantity [30]. The three dimensional solution, $\mathbf{u}^{\mathrm{f}}(r,3)$, was used to represent the electron with the product field $\mathbf{u}^*(r)\mathbf{u}(r)$ representing the electrostatic **E** field [1]. In this derivation charge is quantized based on dimensions. For the case of the nuclear strong force the product $\Phi^*_{\text{strong force field}}\Phi_{\text{strong force field}}$ will be used to represent the strong force fields for the proton and neutron in a product of their component quarks.

$$\Phi_{\text{strong force field}} = \mathbf{u}^{\text{f}}(r,1)\cdot\mathbf{u}^{\text{f}}(r,1D \text{ or } 2D)\cdot\mathbf{u}^{\text{f}}(r,2D). \tag{3}$$

The strong force field is treated as a simple static field, with no color boson, gluon, or exchange binding the components. The individual components are considered bound because only as a whole do they define their existence in the three dimensional laboratory frame, referenced to a common origin. No momentum distribution function for the quarks is considered that treat them as individual dynamic elements. The experimental justification for this is that the proton has no permanent or induced electric dipole moment, even though the component quarks possess spin and charge.

5. The Two-field Problem

Unlike the electron, the proton has two major fields: strong force and electrostatic. By analogy to the electron the massive fermion field made of three quark components support the strong force. We know the electrostatic field of the proton is very different from the electrons as on the mass scale the charge distribution of the proton is significantly larger because of its relative larger magnetic moment. The proton also has the boson characteristic of a weak charge. The proton's weak charge Q_{weak} exists and has been measured in spin-dependent electron scattering experiments off protons [41]. That implies that the proton is not only made up of fractional fermion components to generate the strong force, but also massive boson components to generate the electrostatic field and charge. The proton's lower mass relative to the neutron also implies the energy in the proton's electrostatic field may be proportionally lower as compared to the electrons which is $\sim 0.1\%$ of the total self energy [2]. This indicates a less compact charge density for the proton. Finally, the ability of deuterium to fuse under relatively modest conditions implies that the charge radius of the proton is indeed large.

Table 3. Spatial solutions, $u^{\text{family}}(r, \text{dimension})$, to the particle and field equations of the self-reference frame that generates the boson and fermion families for both massless fields and particles with mass [2,30]. The massive components are in boldface and the massless fields are not in boldface.

Dim.	Boson	Fermion	Note
No mass	Field	Field	
1	$u^{\text{b}}(r,1)$	$u^{\text{f}}(r,1)$	Bound
	Field formation	Neutrino formation	
2	$u^{\text{b}}(r,2)$	$u^{\text{f}}(r,2)$	Bound
3	$u^{\text{b}}(r,3) \rightarrow$ Photon	$u^{\text{f}}(r,3) \rightarrow \nu_e$	Free
Mass	Particle	Particle	
1	$\mathbf{u}^{\text{b}}(r,1)$	$\mathbf{u}^{\text{f}}(r,1) \rightarrow$ Down quark	Bound
	Charge formation		
2	$\mathbf{u}^{\text{b}}(r,2)$	$\mathbf{u}^{\text{f}}(r,2) \rightarrow$ Up quark	Bound
3	$\mathbf{u}^{\text{b}}(r,3) \rightarrow W^{\pm}\, Z^{o}$	$\mathbf{u}^{\text{f}}(r,3) \rightarrow$ Electron	Free

The massless form of the state function derived in equation 4 in the self-reference frame generates solutions dependent on dimension [30]. The 3D solution for the boson represents the photon, whereas, the 3D fermion solution represents the electron neutrino. The lower dimensional massless boson solutions will be used to assemble the long range field and the massive lower dimensional boson solutions will be used to generate the charge. These composite particles are more complex than the three dimensional case because they may require two static fields.

$$\frac{\partial^2 u(r)}{\partial r^2} + \left(\frac{n-1}{r}\right)\frac{\partial u(r)}{\partial r} + \kappa^2 \gamma u(r) = 0. \tag{4}$$

The massless field solutions respectively for the fermion and boson are:

$$\begin{aligned} u^{\mathrm{f}}(r,n) &= \mathrm{e}^{-i\kappa r}{}_1F_1\left[\frac{n-1}{2}, n-1, 2i\kappa r\right], \\ u^{\mathrm{b}}(r,n) &= \mathrm{e}^{-i\kappa r}U\left[\frac{n-1}{2}, n-1, 2i\kappa r\right]. \end{aligned} \tag{5}$$

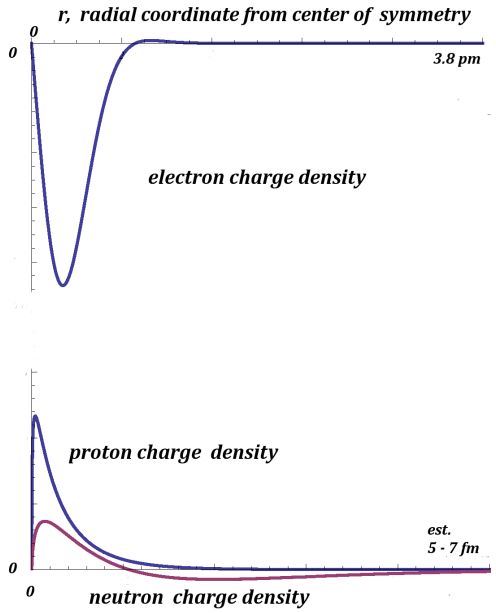

Figure 3. Computed electron, proton and neutron charge densities from self-reference frame state product functions. The neutron total charge is always zero independent of the quark component scales, whereas the proton charge is only totally positive when the up quarks have a scale difference of 2 or greater. Note the two radial scales are in pico meters for the electron and femto meters for the nucleons, their relative heights are set only for visual separation.

5.1. Generating charge density

The electron being a 3-D elementary particle its charge density is generated from, Gauss's law, the gradient of the electric field that is proportional to $\mathbf{E}(r) \sim u^*(r, n = 3)u(r, n = 3)$. This charge density when used to correct the hydrogen's atom Schrödinger equation solution using a singular potential, $1/r$, produces the bulk of the correction of the 1S state $\sim 99\%$ without a need for quantum electrodynamics [1]. This gives us some confidence that these structural solutions for particle composition are correct, Fig. 2.

The proton is a much more complex object with both a strong force field and electrostatic field. The fermion fractional quark solutions appear to generate the compact strong force potential. However, to generate the long range electrostatic field and its supporting charge the two sets of fractional boson components are required. The massive fractional boson components to generate the charge and the massless fractional components to generate the $1/r^2$ electric field. Support for this comes from the zero charge generated for the quark combination for the neutron. The neutron charge is always zero and independent of the quark scale ratio. We tested this numerically for a range of quarks scale ratios. This implies the neutron is very different in its ability to interact via the strong force because of this flexibility that is limited for the proton and its scale.

6. Strong Force Binding

The observable pieces of stable elementary matter, $n = 3$, are the electron, photon, electron neutrino. The massive boson $W^{\pm}$, Z^0 though not stable are solutions of equation 1 that have the charge and parity characteristics verified by experiment [30]. The composite structures: nucleons and mesons forms require more complexity to understand their assembly.

There are tests for the particle that can be made. The first test is for parity problems as a function of relative energy. The field elements should behave like a field and not like a particle, while also being stable. As individual fractional elements the lower dimensional components are not complete. However, in combinations of twos and threes they take on characteristics of three dimensional particles and fields that are actually found: mesons and baryons.

A self-reference frame description was given to the proton and neutron using products of one and two dimensional component solutions representing quarks [30]. What motivated these simple product representations for the composite particles is that for the proton there is no measurable electric dipole moment and the strong force is not plagued by parity violation, which these product forms satisfy using a common origin. With no electric dipole moment the ensemble of quarks would share the same center of symmetry. This makes a case for a potential interaction producing the strong force between nucleons as a contact interaction of overlapping density functions. In Table 3 there are no remaining freely propagating boson fields to represent the gluon. A nuclear strong force potential can be constructed from the products of the lower dimensional massive fermion components. The product of the solutions and its complex conjugate produces a density function that can be integrated to give a potential for the strong force. This is similar to how the electrostatic potential of the electron is generated [1]. The difference is the strong force potential is short range because the particle structures are compact, Table 4 and Fig. 4.

$$\mathbf{u}_{\text{proton}}(r) = \mathbf{u}^{\text{f}}(r, 1) \circ \mathbf{u}^{\text{f}}(r, 2) \circ \mathbf{u}^{\text{f}}(r, 2),$$

$$\mathbf{u}_{\text{neutron}}(r) = \mathbf{u}^{\text{f}}(r, 1) \circ \mathbf{u}^{\text{f}}(r, 1) \circ \mathbf{u}^{\text{f}}(r, 2), \tag{6}$$

$$\mathbf{u}_{6-\text{quarks}}(r) = \mathbf{u}^{\text{f}}(r, 1) \circ \mathbf{u}^{\text{f}}(r, 2) \circ \mathbf{u}^{\text{f}}(r, 2) \circ \mathbf{u}^{\text{f}}(r, 1) \circ \mathbf{u}^{\text{f}}(r, 1) \circ \mathbf{u}^{\text{f}}(r, 2).$$

Table 4. Nuclear characteristics.

Property	Cause
Bound independent nucleons	Compact potential
Zero proton dipole moment	Quark dynamics barred No parton distribution function
Nuclear mass defect	Quark Scale adjustment
Short range correlation	Six-quark state
Aggregate binding $A > 2$	Neutron-proton pair's Extend structure

7. Lab Frame Nucleon Structure

The compact strong force structure of the proton is generated from the relation in Eq. (6) allows a potential to be computed. This would be the strong force potential and not the electrostatic potential because it will be very short range. The potential can be computed outside of the core from the following integral.

$$V_{\text{strong}}(r) = \int_{\infty}^{r} \mathbf{u}^{*}_{\text{nucleon}}(x)\mathbf{u}_{\text{nucleon}}(x)\,\mathrm{d}x. \tag{7}$$

When the spin states are considered it is the proton–neutron pairs that allow for stable structures to be assembled.

7.1. Making deuterium

$$\frac{\hbar^2}{2m}\nabla^2\Phi - \frac{\hbar^2}{2mc^2}\frac{\partial^2\Phi}{\partial t^2} + i\hbar\frac{\partial\Phi}{\partial t} = V\left\{1 + \frac{V}{2mc^2}\right\}\Phi. \tag{8}$$

The full relativistic wave equation in the laboratory frame differs in two ways from the Schrödinger equation by having two additional terms [2]. The second order term in time and the quadratic term in the potential that is always repulsive. These are dropped for low energy bound state calculations assuming they are small. For binding the proton and neutron these two terms will not be used in a first approximation to solving the problem, Fig. 4.

Equation (7) computes the nuclear potential that is a simple exponential.

$$V_{\text{strong}}(R) = -V_{\text{o}}\mathrm{e}^{-\frac{2R}{\epsilon}} = -V_{\text{o}}\mathrm{e}^{-\alpha R}. \tag{9}$$

The nucleons' bound state differs a great deal from an atomic model. The reason being is that the nuclear potential is short ranged.

$$-\frac{\hbar^2}{2m}\nabla^2\Phi - V_o e^{-\alpha R}\Phi = E\Phi. \tag{10}$$

Equation (10) is solved in three dimensions for $\Phi(R,\theta,\phi,t) = U(R,\theta,\phi)G(t)$ much like the atomic central force problem. The method is laid out in [26] where first the angular variables are separated from the radial variable with

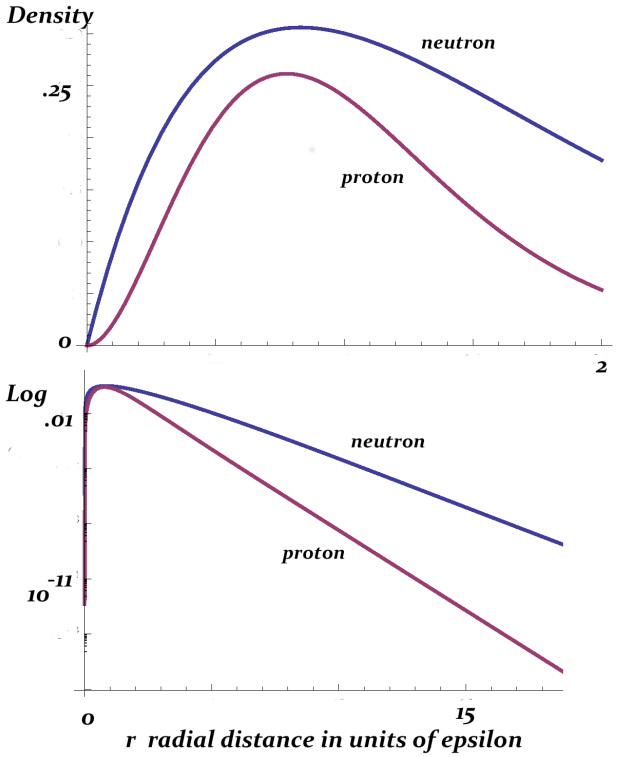

Figure 4. Computed proton and neutron density functions. Where density for the proton $\rho_{\text{proton}} = \mathbf{u}^{*\text{f}}(r,1)\mathbf{u}^{\text{f}}(r,1)\mathbf{u}^{*\text{f}}(r,2)\mathbf{u}^{\text{f}}(r,2)\mathbf{u}^{*\text{f}}(r,2)$ $\mathbf{u}^{\text{f}}(r,2)\ r^2$ from the three quark components and for the neutron $\rho_{\text{neutron}} = \mathbf{u}^{*f}(r,1)\mathbf{u}^{\text{f}}(r,1)\mathbf{u}^{*f}(r,1)\mathbf{u}^{\text{f}}(r,1)\mathbf{u}^{*f}(r,2)\mathbf{u}^{\text{f}}(r,2)\ r$.

separation constant, $l(l+1)$, that turns out to be in terms of the angular moment, l. The solutions with orbital angular momentum are defined in terms of the spherical harmonic functions, which in the nuclear strong force problem can be used to generate the nuclear quadrupole moment. Another force active in deuterium is the interaction of magnetic moments between the proton and neutron. Deuterium binding problem would not be complete unless details of the quadrupole moment were included. Traditionally the quadrupole momentum in deuterium is explained by the mixing of an *S* state and a *D* state in the bound potential [42]. Here the $l = 2$ angular solution mixed with the $l = 0$ principal solution generates the quadrupole moment for those nuclei with non-zero total spin

It is the radial solution, $l = 0$, that is of most interest $U(R,\theta,\phi) \longrightarrow \Phi(R)$ for the ground state. After separating variables an expression for three potential terms are missing: the electrostatic, the magnetic spin–spin interaction and spin–orbit interaction. For deuterium only one of these terms is important and that is the spin–spin interaction.

$$-\frac{\hbar^2}{2m}\left(\frac{\partial^2\Phi}{\partial R^2}+\frac{2}{R}\frac{\partial\Phi}{\partial R}\right)+\frac{l(l+1)}{R^2}\Phi - V_{\text{o}}\,\text{e}^{-\alpha R}\Phi = E\Phi. \tag{11}$$

This analysis starts by assuming the strong force potential term is dominant between a proton and neutron because of the overlapping unpaired *u* and *d* quarks. This is not a bad assumption because the orbital angular momentum in most

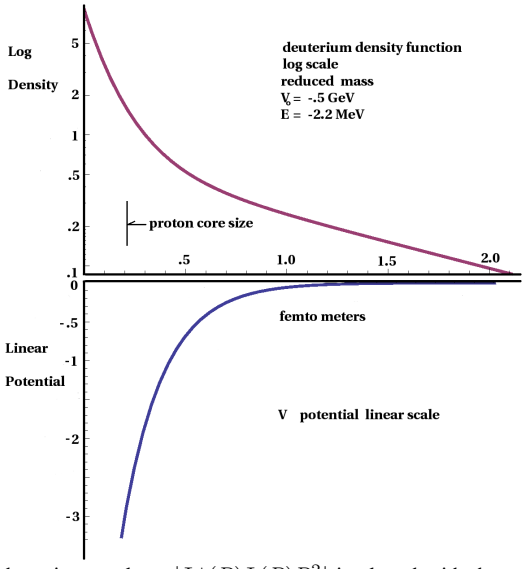

Figure 5. Density function of bound deuterium nucleus, $|\Phi^*(R)\Phi(R)R^2|$ is plotted with the potential. Figure from *yes Virginia, quantum mechanics can be understood* [2].

stable nuclei is zero. This forces a spherical symmetry on the bound state solutions with a central force while ignoring the spin–spin interaction (Fig. 5).

The solutions produced are in terms of the Bessel function $I_\nu(z)$ and $K_\nu(z)$. Only $I_\nu(z)$ solution represents a bound state as $K_\nu(z)$ continues to grow with *R*.

$$\Phi(R) = A\,\frac{1}{\alpha R}2^{\frac{1}{2}-i\frac{\sqrt{2mE}}{\hbar\alpha}}\left(\mathrm{e}^{-\alpha R}\right)^{-i\frac{\sqrt{2mE}}{\hbar\alpha}} \times\left(-\frac{2mV_\mathrm{o}\mathrm{e}^{-\alpha R}}{\hbar^2\alpha^2}\right)^{-i\frac{\sqrt{2mE}}{\hbar\alpha}} I_{-2i\frac{\sqrt{2mE}}{\hbar\alpha}}\left(2\frac{\sqrt{2mV_\mathrm{o}\mathrm{e}^{-\alpha R}}}{\hbar\alpha}\right). \tag{12}$$

The nuclear binding of deuterium is determined by the nucleon mass defect driven by the core overlap of the two nucleons. Whereas, for the bulk of the volume the nucleons behave as single well defined particles. This is expected because the narrow nuclear potential will force the wave function to extend away from the center of symmetry in a second slower decaying exponential. The scale of the bound state is large relative to the individual nucleon core radii. This structural feature may aid deuterium fusion at a close approach.

Setting $\beta = \sqrt{E/2mc^2}$, where β is small >10^{-4} then the density function reduces to

$$\Phi^*(R)\Phi(R)R^2 = \frac{A^*A}{2}\epsilon^2 I_{2i\beta}\left(2\mathrm{e}^{-\frac{R}{\epsilon}}\sqrt{\frac{V_\mathrm{o}}{2mc^2}}\right)\times I_{-2i\beta}\left(2\,\mathrm{e}^{-\frac{R}{\epsilon}}\sqrt{\frac{V_\mathrm{o}}{2mc^2}}\right). \tag{13}$$

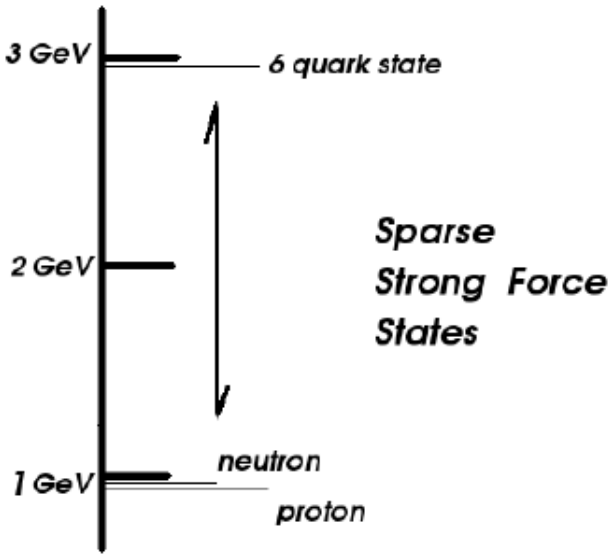

Figure 6. Combined six-quark state showing the sparse distribution of prompt baryon states.

8. High Energy Proton–Neutron State

From electron–nucleon scattering experiments to detect nuclear short range correlation both the internal momentum of nuclear components and the threshold for strong proton-neutron short range correlations can be extracted [40]. This momentum data matches the modeling of deuterium in the previous section for the strong force calculation showing a double exponential decay in both the real and momentum space density functions [30]. These experiments also eliminate any possibility of there being deep state electrons in the structure as they would be easily detected in the scattering experiments.

Using statistically independent spaces for particles and fields forced the abandonment of the point particle descriptions and replaces it with a structured particle properties. This allows including the nucleon's component quarks to form high energy compact particles totally unlike the low energy elementary three dimensional lepton, electron. Particle structure overlap for nucleons can be computed to generate the strong force's static potential function. Models using an exchange of boson analogous to photon emission and absorption do not appear to be required for either binding or in modeling scattering experiments.

The use of this simple model in the case of deuterium has proven useful in both being able to define binding of the two nucleons [2] and defining the high energy state when the proton is driven into the neutron to form the short range correlated structure. This latter condition computed from the excess energy, 1 GeV, required to form a six quark state shown in Fig. 6. This energy is taken from the reduced scale of the six-quark state. The excess energy required for the high energy state comes from the reduced scale the entire structure and is the simplest behavior that occurs promptly on collision. The six-quark state will not form until an extra 1 GeV of energy can be externally supplied either by an accelerator driven collision or in a massive astrophysical object, a neutron star near its upper mass limit (Fig. 7).

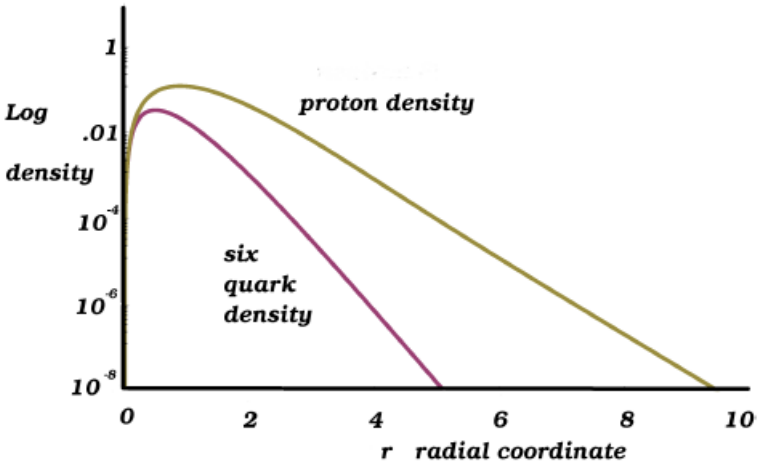

Figure 7. Scale reduction to the six-quark state is a factor three, not two and that requires an extra 1GeV over the rest energy of the two nucleons to be accomplished.

8.1. Nuclear short range correlation for heavier isotopes

Schematically the momentum space data from the short-range correlation experiments can be represented in a simple graph that has three parts [40]. The first part is the dominate low momentum peak in the deuterium data where the nucleons spend some of their time with low momentum with no third particle constraints limiting their motion. As

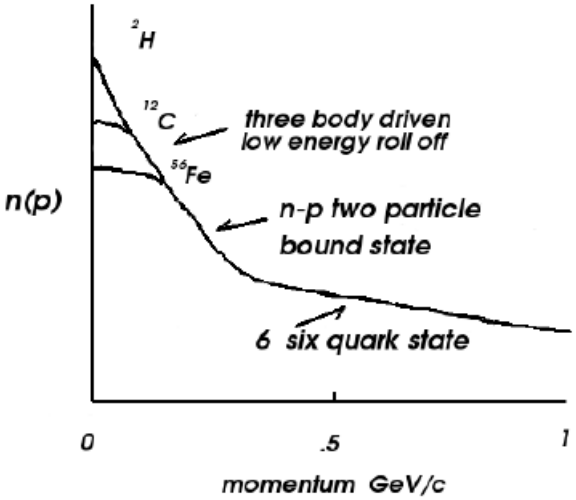

Figure 8. Measured log momentum density from high energy electron scattering not only shows the n–p correlation for deuterium, but the confinement effect of the three body interaction at high nucleon counts in the roll off of the zero momentum peak [40].

nucleons are added the low momentum behavior around $p = 0$ is suppressed as other two body interaction occur. The unchanging intermediate momentum for increasing nuclei count suggestion this behavior is universal as isotope mass is increased squeezing down region in the middle section in Fig. 8. The third high momentum region remains a fixed feature is the short-range correlation in the high energy tail. Over this wide energy range the spectroscopy is not very rich, meaning there are few available states other than the two particle interactions and the six-quark state. This is very different when compared to solid state models with a high density of states that are commonly misused to model nuclear matter.

8.2. Implications for binding $A > 2$

The implication from more recent accelerator experiments [43] probing the nucleus with electrons allows nuclear binding to be reduced to a structure dependent property, without considering deep states that do not exist or meson binding intermediaries. By finding the first prompt state of deuterium at $\sim$1 GeV above the self-energy of deuterium when the proton and neutron are forced to be one removes a great deal of confusion. Then electron probing below this threshold for short range correlation, which translates to less than $\sim$4.5 GeV for the electron input energy permits the internal momentum distribution of the proton in deuterium and heavier nucleons to be more accurately probed. This yields a picture of the deuterium density function than can be consumed in binding with additional nucleons.

The deuterium nucleus in Fig. 5 shows two distinct regions: a well defined core and a wider regions extending outwards. It is the broader structure that represents the low momentum values of the nucleons that can interact and attract other nucleons. Though this portion of the density function only represents 10% of the particle's density, its reach allows other nucleons and other proton-neutron pairs to bind. Evidence can be seen in data of recent accelerator experiment measuring the momentum distribution for knocked out protons from deuterium, tritium, and ^{3}He, as the exterior portion of the deuterium wave function is consumed in the binding of the additional nucleon [43]. This data is recorded as the ratio in cross section of protons knocked out from tritium and ^{3}He scale to deuterium at the minimum measured internal proton momentum. This measured ratio is well less than 1 in tritium and ^{3}He indicating the low momentum or spatially extended part of the wave function of deuterium has been truncated and now forms a bond with greater particle momentum. This was also evident in the early short range correlation measurements for heavier nucleons as shown in Fig. 8. The conclusion is that the proton–neutron pair constitutes the basis to build heavier nucleons because of their extended structure and facilitates fusion.

9. D–D Fusion

Standard D–D fusion proceeds on two equally probable paths if there is sufficient energy to drive the ions together in free space.

$$\begin{aligned} {}^2\mathrm{H} + {}^2\mathrm{H} &\rightarrow {}^3\mathrm{H} + \mathrm{n} + 17.6\ \mathrm{MeV}\ \ 50\%, \\ {}^2\mathrm{H} + {}^2\mathrm{H} &\rightarrow {}^3\mathrm{He} + \mathrm{p} + 4.03\ \mathrm{MeV}\ \ 50\%. \end{aligned} \tag{14}$$

One feature of D–D fusion reaction found in D–D scattering cross section data is that no abrupt lower bound cut off for fusion as a function of colliding particle energy is found. The important feature allowing fusion is that both energy and momentum are conserved requiring multiple final state products. The process in question, Eq. (15) does not have this pathway to conserve both energy and momentum unless there is some other element to carry off the energy. Gamma emission is suppressed in low energy encounters. That only leaves an external particle participating to carry off the energy and momentum.

$$^2\mathrm{H} + {}^2\mathrm{H} \rightarrow {}^4\mathrm{He}^* + \sum_i \Delta E(e_i) \rightarrow {}^4\mathrm{He} + \text{heat}. \tag{15}$$

For free particle interaction this third process is not observed as there is nothing to remove the 24 MeV excess energy. The first two reaction are not dominant in the solid state as the quantities of tritium and helium-3 are only found in trace amounts, whereas, there are significant correlated findings of both helium-4 and heat.

9.1. Loss mechanism

During nuclear fusion when a proton and neutron combine, the masses of the components are reduced and the excess energy will be shed. The electrostatic field of the proton and neutron will be altered in the region of the core even though its charge remains constant. The change in the charge distribution and associated energy change is absorbed in the mass change allowing energy to be shed directly to lattice electrons coupled to the change in baryon charge density distribution through the electrostatic field. This can be represented as a time dependent interaction potential, $V_{\text{int}}(t)$.

$$V_{\text{int}}(t) \sim \iint \frac{\rho_{\text{electron}}(r)\rho_{\text{baryon}}(r',t)}{\mid \mathbf{r} - \mathbf{r}' \mid} r'^2 r^2 \mathrm{d}r' \, \mathrm{d}r. \tag{16}$$

If the mass defect energy from fusion can be acquired by electron currents local to the nucleus then the normal fusion processes will be short circuited and the energy will be deposited into the valence electrons. Nickel and Palladium possess a band structure, a characteristic not shared by any other metals to allow this process.

9.1.1. *Nuclear polarization*

The scale of the electron charge sets the minimum range where dynamic screening is effectively provided by the valence electron and this is on the order of 4×10^{-13} m. To further close this range the non-linear response of the lattice so that the nuclear attraction can overcome the electrostatic repulsion. It is only possible to estimate the cross over point once the charge structure of the nucleus is known as well as the strong force polarization.

The incremental energy transfer to valence electron current is not a quantized process because the energy states of the nucleus are dependent on the scale relationship between the nucleon quarks, which appear to vary continuously. The low levels of residual radiation from tritium production indicates that the incremental loss of energy to the lattice is the most active component and it rarely produces a single high energy transition to a lattice electron carrying MeV energy. The flexibility that is obtained in the incremental energy loss is due to the three-body behavior of the quark's scale in adjusting nucleon mass. The neutron is the most compliant in terms of energy verses its quark scaling. This compliance lets the internal quark scale adjustments bind nucleons in the fusion process [2]. Compliance means that the up-down quark scale ratio can vary more for a smaller change in nucleon rest energy in the neutron verses the proton.

Interrupting the loss process requires the question to be asked: Is the energy transference reversible? The answer to this is that it is improbable because it would require extraction of energy from the valence electrons at the prevailing temperature. The local heat capacity in the electron gas is insignificant when compared with the energies involved in the nuclear process. This makes the reversal of the process highly unlikely in terrestrial environments.

The scale over which this process occurs is fixed by the details of the approach of the two nucleons to minimize the electrostatic potential and maximize the strong force attraction. EM and weak force polarization is understood and that has to be extended to the strong force. In the schematic of the approach of two deuterium ions shown in Eq. (17), the lower figure would represent a favorable polarization for fusion.

Table 5. Guide to the sequence of events that lead to fusion in the FCC lattice and the dumping of heat into the lattice by a direct potential interaction between the fusing deuterium ions and dynamics screening currents that are supported in some FCC metals. The number of steps in this process are reflected in the difficulty of engineering a large scale process. Column three represents the mechanically alloyed Ni–Pd interface and the diffusion Ni–Cu boundary.

▼	$\Longleftarrow$ Damage Controlled	
	Mechanical alloying controlled $\Longrightarrow$	▼
1	Absorption of deuterium into Pd, Ni, or Ti	1
2	Strong near surface $> 1\mu$m damage gradient	
3	Hydride formation, bulk lattice expansion, stacking fault generation (Ti)	
4	Vacancy formation and coalescence into microvoids	
5	Damage and hydride forced expansion of the untransformed volume	
6	Deuterium wetting of interior of microvoids	
7	Microvoid collapse into prismatic dislocation loop	
8	Microvoid collapse ejecting ^{2}H ions into local matrix	
	Mechanically alloy Ni–Pd interface Ni–Cu diffusion boundary	2
9	Dual ^{2}H ions split on a $\langle 111 \rangle$ axis centered symmetric FCC octahedral site	3
10	Symmetric closed die forge, compression enhanced by anharmonic lattice vibrations	4
11	Dynamic screening of dual ^{2}H ions by valence electron 6-axis current flow	5
12	Overlap of neutron and proton wave function releases energy to screening currents	5
13	Adjustment of nucleon charge distribution via potential interaction to screening currents	7
14	Irreversible energy shedding to the current as proton charge distribution adjusts	8
15	Final energy transfer via a potential interaction interaction with screening electrons	9
16	Lattice supported D–D fusion	10

$$\begin{aligned} \{\mathbf{N}-\mathbf{P}\} \dashrightarrow \quad \dashleftarrow \{\mathbf{N}-\mathbf{P}\}, \\ \{\mathbf{P}-\mathbf{N}\} \dashrightarrow \quad \dashleftarrow \{\mathbf{N}-\mathbf{P}\}. \end{aligned} \tag{17}$$

The question is what kind of attractive force is generated between two neutrons already in a bound structure?

This is expected to be very different than what is found between two free neutrons. A reflection of this can be found in the old accelerator measurements that searched for a threshold in D–D fusion, none was found, only a roll off in cross section as interaction energies fell below 10 keV. At these low energies the force amplification on the interstitial site from anharmonic [21] localization of lattice vibration can drive the fusion process to completion assisted by the increasing nuclear attraction as the excess energy is removed by electronic currents (Table 5).

10. Discussion

The importance of the experimental cold fusion work started by Fleischmann and Pons [8] opened a window on the workings of the nucleus where a unique low energy view is supplied. Before a serious examination of the nucleus and cold fusion could take place the problems with quantum mechanics had to be resolved: structure of the participating components and polarization [44]. It was known since the early 1930s that quantum mechanics was in need of a serious overhaul [27,45–48]. The strong force is the most complex of the forces and the most difficult to handle. The barrier to modeling cold fusion was a poor understanding of the strong force, because of the binding mechanism the standard model tried to impose. Specifically, the requirement for a fictitious complex field called the gluon. Once the gluon was discarded it was possible to look at the lattice fusion process in detail after the metallurgical preliminaries were clarified. For the more general problems of particle physics the mechanisms used for assembling the baryons and their respective charges out of fractional fermion and boson components opens a path for building the other family of particles.

The minimal D–D fusion process in metals requires a complex chain of events (Table 5) with a favorable crystal and band structure making the process difficult to trigger. The recent accelerator experimental evidence of external electrons directly participating in the nuclear fusion process [33] added the lattice electron as a candidate to mediated nuclear fusion to the standard processes of transmutation: alpha, beta, electron capture, fission, and gamma emission. The solid state fusion process of two deuterium ions occupying a single FCC octahedral interstitial site presents some experimental challenges, because the residence time is probably a picosecond or less. A signal to the process was found in the spectrum of electromagnetic radiation that is normally a very weak emission that appears to be pumped by intense screening currents in M. Swartz active MASER at 327 MHz. The triplet to single transition from lattice bound atomic deuterium being strongly pumped by local currents in an active cold fusion specimen Pd–D embedded in ZrO_2 provides some proof of the role of electronic currents in the loss mechanisms driven by lattice fusion.

Acknowledgments

The most important source of information for this paper were the many failed attempts to generate physical results as this large body of work narrowed the range of possible mechanisms.

References

[1] J. Wallace and M. Wallace, Electrostatics, in: G. Meyneni(Ed.), *Science and Technology of Ingot Niobium for Superconducting Radio Frequency Applications*, AIP Conf. Proc., Vol. 1687 (AIP Melville, NY 2015) 040004-1-14.

[2] J. Wallace and M. Wallace, *yes Virginia, Quantum Mechanics can be Understood*, Casting Analysis Corp., Weyers Cave, VA, 2017.

[3] A. Carpinteri, G. Lacidogna and A. Manuello (Eds.), *Acoustic, Electromagnetic, Neutron Emission from Fracture and Earthquakes*, Spriner, Switzerland, 2015.

[4] G. Egely, Transmutation by dust fusion, *Infinite Energy* **130** (2016) 19–25.

[5] L. Jaitner, *The Theory of Condensed Plasmoids and Low Energy Nuclear Reactions*, preprint, www.condensed-plasmoids.com 2015–2019.

[6] Borexino Collaboration, Comprehensive Measurement of pp-chain solar neutrino, *Nature* **562** (2018) 505–510.
[7] J.P. Wallace and M.J. Wallace, *Refraction*, 2018, http://viXra.org/pdf/1809.0582v2.pdf.
[8] M. Fleischmann, S. Pons and M. Hawkins, *J. Electroanal. Chem*. **261** (2A) (1989) 301.
[9] Y. Iwamura, S. Murakami and J. Kasagi, Excess energy genertion using a nano-sized multilayer metal composite and hydrogen gas, *J. Condensed Matter Nucl. Sci.*, submitted.
[10] T. Mizuno and J. Rothwell, Increased excess heat from palladium deposited on nickel, preprint, https://www.lenr-canr.org/acrobat/MizunoTexcessheat.pdf.
[11] F. Celani, C. Lorenzetti, G. Vassallo, E. Purchi, S. Fiorilla, S. Cupellini, M. Nakamura, P. Boccanera, R. Burri and A. Sapllone, First evaluation of coated constantan wires comprising Capuchin knots to increase anomalous heat and reduce input power at high temperature, *J. Condensed Matter Nucl. Sci.* **29** (2019) 52–74.
[12] Y. Fukai and W. Okuma, Formation of superabundant vacancies in Pd hydride under high pressures, *Phys. Rev. Lett.* **73** (1994) 1640–1643.
[13] E. Storm, Anomalous energy produced by PdD, *J. Condensed Matter Nucl. Phys.* **20** (2016) 81–99.
[14] K. Sakai, M. Mizuno, H. Araki and Y. Shirai, The effect of the hydrogenation process on the production of lattice defects in Pd, *J. Alloys Compounds* **414** (2006) 204–206.
[15] J. Wallace, *Positron Interactions with Vacancies and Dislocations*, D. Eng. Sc., thesis, Columbia Univ. NY, 1975.
[16] R. Golpaliengar, J. Wallace and R. Oriani, *Mat. Sci. Eng*. **85** (1984) 191.
[17] M. Swartz, Atomic deuterium in active LANR systems produce 327.37 MHz Superhyperfine RF MASER emission, ICCF-22 Abstract, Sept. 2019.
[18] J. Li, R. Oriani and L. Darken, The thermodynamics of stressed solids, *Zeit. Phys. Chem.* **49** (1966) 271–290.
[19] M. Swartz, *J. Condensed Matter Nucl. Sci.* **15** (2015) 102–105.
[20] M. Swartz, G. Verner, J. Tolleson, L. Wright, R. Goldbaum and P. Hagelstein, *J. Condensed Matter Nucl. Sci.* **15** (2013) 66–80.
[21] V.I. Dubinko and D.V. Laptev, Chemical and nuclear catalysis driven by anharmonic vibrations, *Lets. Materials* **6**(1) 16–21.
[22] J. Wallace, Proton in SRF niobium, in G. Myneni (Ed.), *SSTIN10 AIP Conference Proc. 1352*, AIP, Melville, NY, 2011.
[23] J. Wallace, G. Myneni and R. Pike, Curvature, Hydrogen, and Q, in: G. Myneni(Ed.), *SSTIN10 AIP Conf. Proc. 1352*, AIP, Melville, NY, 2011, pp. 33–46.
[24] J.P. Biberian, Transmutations, *J. Condensed Matter Nucl. Sci.*, 2019, to be published.
[25] R.W. Cahn, Recovery and recrystallization, in: R.W. Cahn(Ed.), *Physical Metallurgy*, North-Holland, Amsterdam, 1970, pp. 1129–1198.
[26] H. Bethe and E. Salpeter, *Quantum Mechanics of One- and Two-Electron Atoms*, Springer, Berlin, 1957.
[27] P. Dirac, *Relativistic quantum mechanics*, *Proc. Royal Soc.* **A 136** (1932) 453.
[28] H. Foley and P. Kusch, *Phys. Rev.* **73** (1948) 412.
[29] W. Lamb, *Phys. Rev.* **72**(3) (1947) 241.
[30] J. Wallace and M. Wallace, *The Principles of Matter Amending Quantum Mechanics*, Casting Analysis Corp., Weyers Cave, VA, 2014.
[31] V. Moruzzi, J. Janak and A. Williams, *Calculated Electronic Properties of Metals*, Pergamon, NYC, 1978.
[32] P. Kalman and T. Keszthelyi, Solid state internal conversion, *Phys. Rev. C* **69** (2004) 031606(R).
[33] M. Liboglavsek, *J. Condensed Matter Nucl. Sci.* (2019) to be published.
[34] J. Dauben, *George Cantor His Mathematics and Collaboration*, Harvard Univ. Press, Cambridge, MA, 1979.
[35] G. Cantor, *J. für die reine und angewandte Mathematik* **84** (1887) 242.
[36] W. Heisenberg, *The Physical Principles of the Quantum Theory*, Univ. Chicago Press, Chicago, IL, 1930.
[37] J. von Neumann, *Mathematical Foundations of Quantum Mechanics*, Princeton Univ. Press, 1932, translation 1953.
[38] J. Friedman and H. Kendall, Deep inelastic scattering, *Ann. Rev. Nucl. Sci.* **22** (1972) 203–254.
[39] M. Gell-Mann, Symmetries of baryons and mesons, *Phys. Rev.* **125** (1962) 1067–1084.
[40] J. Arrington, D. Higinbotham, G. Rosner and M. Sargsian, Hard probes of short-range nucleon–nucleon correlations, 2012, arXiv:1104.1196v3 [nucl-ex].
[41] Q_{weak} Collaboration Jefferson Lab., *Nature* **557** (2018) 207.
[42] E. Fermi, *Nuclear Physics*, (Univ. Chicago Press, Chicago, IL 1949.

[43] Tritium Collaboration Jefferson Lab. Hall A, Comparing proton momentum distribution in $A = 2, 3$ nuclei via ^{2}H, ^{3}H, and ^{3}He (e,e'p) measurement, arXiv 1902.06358v3 [nucl-ex] (2019).
[44] J. P. Wallace and M.J. Wallace, Refraction, http://viXra.org/pdf/1809.0582v3.pdf, 2018.
[45] G. Gamow, *Thirty Years that Shook Physics*, Anchor Books, NY, 1966.
[46] A. Einstein, B. Pololsky and N. Rosen, *Phys. Rev*. **47** (1935) 777.
[47] Y. Aharonov and D. Bohm, *Phys. Rev*. **115** (1959) 485.
[48] J. Bell, On Einstein, Polodsky, and Rosen Paradox, *Physics* **1**(3) (1964) 195.
[49] J. Wallace, G. Myneni, M. Wallace, R. Pike and G. Westphal, *Terrestrial Nuclear Processes*, Casting Analysis Corp., Weyers Cave, VA, 2012.

J. Condensed Matter Nucl. Sci. 30 (2020) 25–35

Research Article

First Evaluation of Coated Constantan Wires Incorporating Capuchin Knots to Increase Anomalous Heat and Reduce Input Power at High Temperatures

Francesco Celani*,†, C. Lorenzetti, G. Vassallo‡, E. Purchi, S. Fiorilla, S. Cupellini, M. Nakamura, P. Boccanera, A. Spallone† and P. Cerreoni

International Society for Condensed Matter Nuclear Science (ISCMNS-L1), Via Cavour 26, 03013 Ferentino (FR), Italy

B. Ortenzi

INFN-LNF, Via E. Fermi 40, 00044 Frascati (RM), Italy

R. Burri

Innovative Energy Technology Laboratory, Via Somana 6, 6827 Brusino Arsizio, Switzerland

Abstract

Anomalous Heat Effects (AHE) have been observed in wires of $Cu_{55}Ni_{44}Mn_1$ (Constantan) exposed to H_2 and D_2 in multiple experiments during the last eight years. Improvements in the magnitude and reproducibility of AHE, and improvements in wire preparation and reactor design were reported by the authors in the present and previous papers. The oxidation of the wires by pulses of electrical current in air creates a rough surface featuring a sub-micrometric texture that proves particularly effective at inducing thermal anomalies when temperature exceeds 400°C. This effect appears also to be increased substantially by deposing segments of the wire with a series of elements (such as Fe, Sr, Mn, K, via thermal decomposition of their nitrates applied from a water solution). Furthermore, an increase of AHE was observed after placing the treated wires inside a sheath made of borosilicate glass (B–Si–Ca; BSC), and even more after impregnating the sheath with the same elements used to coat the wires. (continued in the next page)
 ISSN 2227-3123

Keywords: Air-flow calorimetry, Anomalous Heat Excess (AHE), Electro-migration phenomena, H_2 →2H dissociation by Constantan, H_2 and/or D_2 absorption at high temperatures into Constantan, Low work function materials, Noble gases, Plasma surface interaction, Spontaneous voltage generation along hydrogen-absorbing wires, Surface-modified Cu–Ni–Mn alloy

*Corresponding author. E-mail: franzcelani@libero.it.
†Also at: INFN-LNF, Via E. Fermi 40, 00044 Frascati (RM), Italy.
‡Also at: Department of Ind. and Dig. Innov., University of Palermo, Viale delle Scienze, 90128 Palermo (PA), Italy.

© 2020 ISCMNS. All rights reserved. ISSN 2227-3123

(continued from the title page)

The treated wire, comprised of knots and sheaths, was wound around a SS316 rod and inserted inside a thick wall glass reactor. The presence of thermal and chemical gradients is an important factor, especially when considering the noteworthy effect of knots on AHE. The ICCF21 Conference held in June 2018 marked a turning point, when the scientific community showed notable interest in the effects of knots and wire treatments, further increasing confidence in the approach. From that time on, attempts to further increase AHE focused on the introduction of different types of knots, leading to the choice of the "Capuchin" type. This knot design produces very hot spots along the wire and it features three areas characterized by a temperature difference up to several hundred degrees. Efforts were also made to better understand the thermionic effect of the wire, and the spontaneous voltage that arises when a second wire is introduced close by (anode). Eventually a large AHE rise was observed when an extra voltage was introduced between the active wire (cathode) and the second wire (anode) through an external power supply; a truly remarkable effect, despite its short duration due to the wire failure caused by an AHE runaway that melted the wire. This article summarizes the presentation given at the 13th International Workshop on Anomalies in Hydrogen Loaded Metals and reports the latest AHE results obtained from a new reactor design comprised of Capuchin knots and new custom manufactured, enhanced sheaths.

1. Introduction

Over the last eight years, our group observed Anomalous Heat Effects (AHE) in wires of $Cu_{55}Ni_{44}Mn_1$ (Constantan) exposed to H_2 and D_2 Constantan (CN) is a cheap alloy that can provide 1.56–3.16 eV for the dissociation of molecular hydrogen and deuterium, whereas the more studied and expensive Pd can only deliver 0.424 eV [1]. Furthermore, Constantan similarly to palladium can absorb a significant amount of hydrogen [2].

Improvements in the magnitude and reproducibility of AHE were reported by the authors of the present work in the past and related to wire preparation and reactor design [3–5]. The oxidation of the wires by pulses of electrical current in air creates a rough surface featuring a sub-micrometric texture particularly effective at inducing thermal anomalies when the wire's temperature exceeds 300–400°C and local non-equilibrium conditions are promoted.

2. Wire Treatment

The AHE appears also to be increased substantially when deposing segments of the wire with a series of elements such as Fe, Sr, Mn, K, via thermal decomposition of their nitrates, applied from a diluted acidic heavy-water solution. This treatment leads to a mixed oxides coating that dramatically change the magnetic properties of the wires. The coating turns the wire from a-magnetic to ferromagnetic. Our group has speculated also that the coil geometry of knots on the wires may further increase the observed magnetism arising from Iron Oxides containing coating. Remarkably, an increase of AHE was observed also after enclosing the treated wires inside a sheath made of borosilicate glass (B–Si–Ca; BSC), and even more after impregnating the sheath with the same elements used to coat the wires (nitrate impregnated sheaths were first dried and later heated to promote the formation of oxides).

Eventually, the AHE was augmented after introducing equally spaced knots to induce thermal gradients along the wire (knots indeed, become very hot spots when a current is passed along the wire).

Interestingly, the coating appears to be nearly insulating and it is composed of mixed oxides of the corresponding elements (mostly FeOx, SrO). After we observed a degradation of the BSC fibers at high temperature, an extra sheath made of quartz fibers was used to prevent the degraded fibers from detaching from the first sheath. Recently the two coaxial sheath assembly has been replaced with a hybrid single sheath developed, in a collaboration between SIGI-Favier and an Italian Metallurgical Company. The latter has not only provided materials, but since 2011 they have also independent cross-checked of some of our results in their own laboratories.

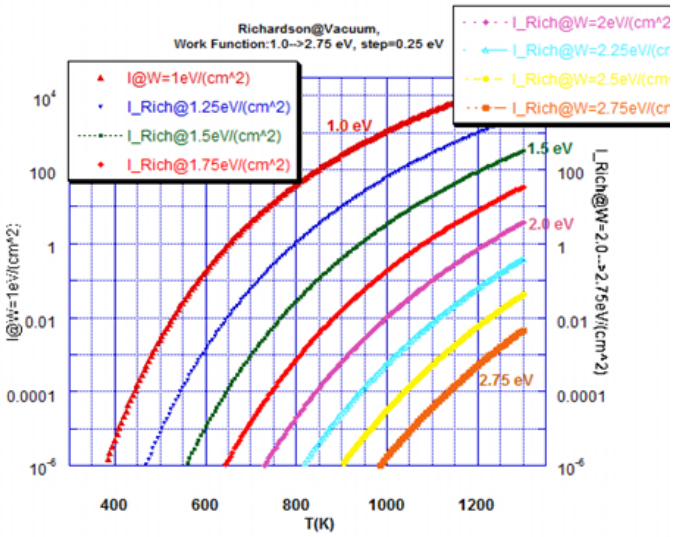

Figure 1. Dependence of electron emission on temperature (300–1300 K) and work function (1–2.75 eV).

The treated wire, comprised of knots and sheaths, was wound around a SS316 tube and inserted inside a thick wall glass reactor. The reactor operates via direct current heating of the treated wire, while exposing it to a 5–2000 mbar of D_2 or H_2 and their mixtures with a noble gas. (In these conditions electromigration phenomena are supposed to occur.)

3. Richardson Law

In 2014, the authors introduced a second independent wire in the reactor design and observed a weak electrical current flowing in it while power was supplied to the first [4]. This current proved to be strongly related to the temperature of the first wire and clearly turned to be the consequence of his Thermionic Emission (where the treated wire represents a cathode and the second wire an anode), in close accordance with the Richardson law.

Also, it must be highlighted that the key parameter of thermionic emission is the work function (Fig. 1); this is usually between 1.5 and 5 eV, and refers to the energy required for the electron emission from a surface:

$$J = A_{\mathrm{g}} T^2 \exp(-\lambda / k_{\mathrm{B}} T),$$

where:

- J the emission current density (A/m^2), Ag= λ_{R}A, λ_{R} is a correction factor depending on the material (0.5–1); A =$(4\pi q_e m_e k_b^2)/(h^3)$ =1.2$\times$ 10^6 (A/m^{2}K^2), Richardson constant
- q_e =1.6$\times$ 10^{-19} C, electron charge; m_e =5.11$\times$ 10^5 eV, electron mass; k_{B} =8.617$\times$ 10^{-5} eV/K, Boltzmann constant.

Our experiments showed that the presence of the thermionic effect and a spontaneous voltage between the two wires is strongly associated with AHE occurrence. This observation led us to find ways to increase electron emission by the deposition of Low Work Function materials (LWFm, such as SrO), on the surface of the Constantan wires.

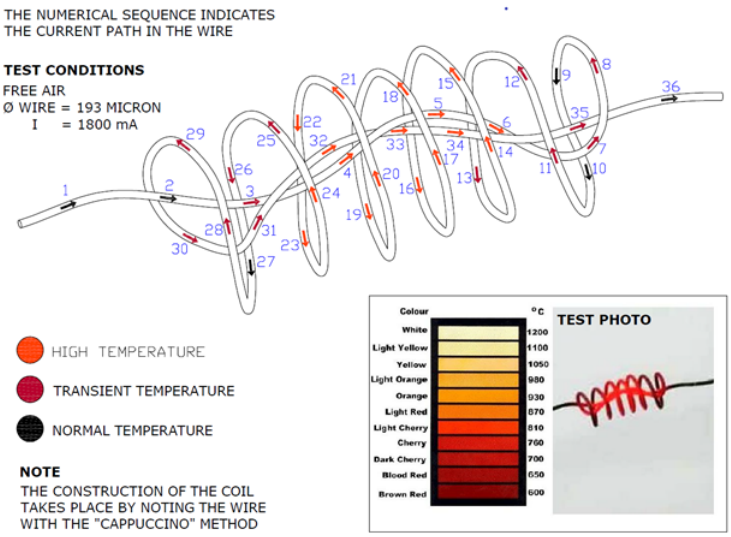

Figure 2. Picture of an eight loop knot heated in air with a direct current ($I = 1800$ mA). Wire of 200 μm diameter. If we estimate the temperature using color, the dark area is likely to be at <600°C, the external spires at about 800°C, while the inmost straight section, may reach 1000°C.

Also, the presence of thermal and chemical gradients is considered as being particularly relevant, especially when considering the large effect of knots on AHE magnitude. These experimental findings were reported at the ICCF21 Conference held on June 2018 and the scientific community showed notable interest in the effects of knots and wire treatments, further increasing the confidence on the described approach.

4. The "Capuchin knot" Geometry

After ICCF21, attempts to further increase AHE focused on the introduction of different types of knots, leading eventually to select the socalled "Capuchin" type (see Fig. 2). This knot design produces very hot spots along the wire and features three areas characterized by a temperature delta up to several hundred degrees. The temperature delta between the external spires of the knot and the internal straight segments may induce also a voltage (V) arising from an Ohmic drop along the wire, and from the different temperature between the inner part of the knot and the external spires. In other words, we may have a significant voltage arises between the relatively cold spires and the internal wire segments (up to 300–400°C hotter than the spires). Taking into consideration this difference of potential, and the emitted electrons from the warmer segments of the wire, we believe that the knot behaves as a diode.

Based on these observations, efforts have been made to better understand the thermionic effect of the wire, and the spontaneous voltage that arises when a second wire is introduced close by (anode). We emphasize that a large AHE rise was noticed when introducing an extra voltage (at low current) between the active wire (cathode) and the second wire (anode) through an external power supply. This is a truly remarkable phenomenon, despite its short duration due to the wire failure (caused by a runaway AHE melting the wire). This effect occurred in particular with 100 μm thick wires, where the voltage drop along the wire may reach 100 V and it is significantly larger with respect to the 200 μm wires. Eventually the authors observed a stunning similarity of the best performing reactor design and a thermionic diode where the active wire represents the cathode and the second wire the anode, whereas the electrodes are separated by fibrous layers impregnated with mixed oxides comprised of iron and alkaline metals.

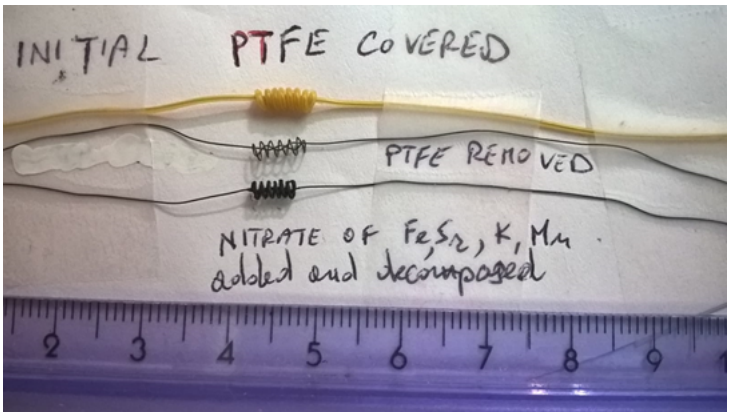

Figure 3. Photo of a typical coil just assembled (*top*), after PTFE destruction (*middle*), after nitrate addition and decomposition to oxides (*bottom*).

In short, preliminary measurements, at reduced pressure, show a current dependence as $V^{1.5}$, resembling the Child–Langmuir law for current emission inside a vacuum diode. The net result of the observations allow us to speculate on a thermionic power converter able to generate electricity through the thermionic emission of a cathode, heated by AHE, and collected by an anode (colder and/or featuring a different work function with respect to the cathode).

5. Preparation of the Knots

The knot preparation starts with a wire of a Constantan variant (Cu55 Ni45) free of manganese. The wire has a PTFE coating (the yellow material shown in Fig. 3). The diameter of Constantan wire is listed in the supplier's specifications as 193 μm We measured it as 197$\pm$3 μm. The external diameter including PTFE is 730 ($\pm$ 5) μm (Fig. 3, top). Decomposition of PTFE sheath is carried out at 550°C in air flow and at 0.15 bar for 10 ks. (Caution: a "water vacuum pump" was used to vent traces of hydrofluoric acid from the decomposition of PTFE). The wires were then dipped in 8% HNO_3 for 5 min and rinsed in distilled water. (Fig. 3 wire in the middle.) Several cycles (5–10) were repeated of deposition of diluted solution of nitrates of Fe, Sr, K, Mn and high temperature decomposition (500–800°C) to oxides. A typical procedure starts with a $\sim$200 cm wire. After preparing the knots (14 knots of eight loops each) the resulting length is $\sim$130 cm.

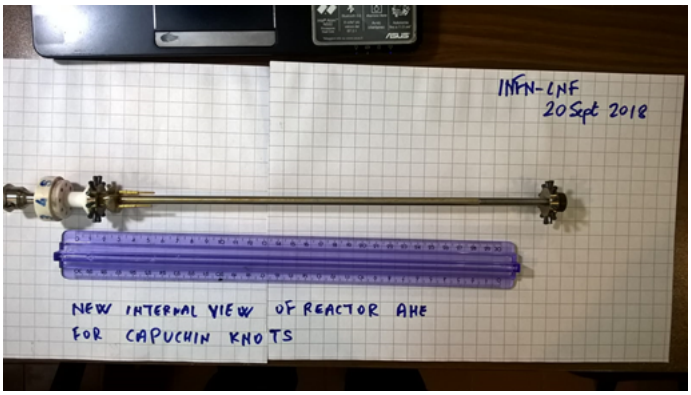

Figure 4. Supports for the wires with knots geometry.

6. Reactor Assembly

The reactor consists of a borosilicate glass tube (D= 33–40 mm, L=400 mm). A central support is used to hold in place wires and their sheaths (Pictures in Figs. 4 and 5). Thermal power was measured with air-flow calorimetry. A calibration was made using an internal tungsten lamp (Figs. 6–8). Details on the calorimetric technique can be found in the ICCF21 presentation.

7. Calorimetry

The air flow calorimeter is calibrated with a tungsten lamp heater (maximum power 230 W), which is under-powered to decrease the emission temperature of the filament. The lamp is inserted into a borosilicate tube with dimensions similar to the active reactor. Both the heater and the reactor are placed in close proximity, and covered by several layers of a 40 μm aluminum foil. The fan is 5 cm wide, operates in suction mode and has a nominal air flow of 4.445 l/s at NPT and 75 Hz. Its rate is monitored (revolutions/second) and logged in the acquisition system (based on a PXIe

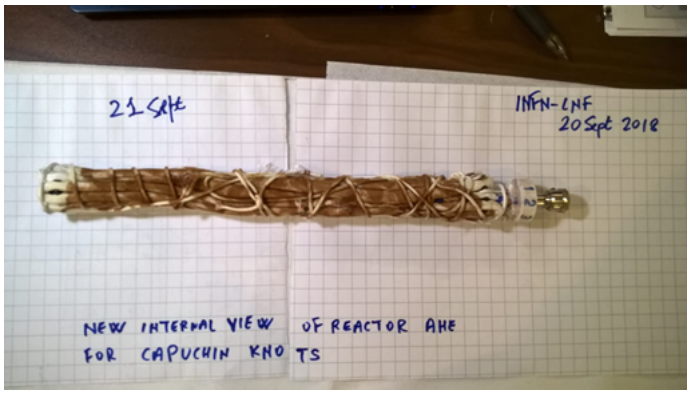

Figure 5. Reactor core, comprised of wires and sheaths made of quartz and borosilicate fibers. This “hybrid” sheath was custom manufactured by SIGI-Favier with the support of a metallurgical company in northeast Italy.

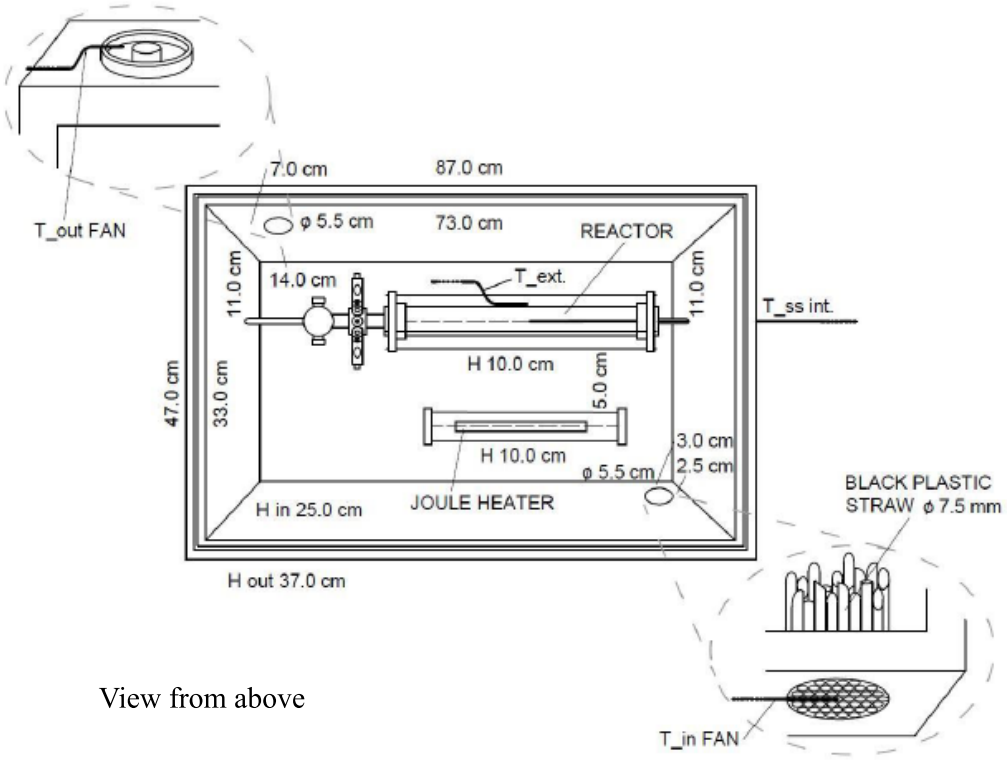

Figure 6. Schematic of the reactor and calorimeter case.

made by National Instruments). The overall average coefficient of heat exchange during calibrations is approximately 0.20°C/W and is consistent with the values of air flux, density, and heat capacity in the range of air temperatures inside the calorimeter (20–60°C). A selection of measurements is reported in Ref. [6] and Table 1 in this work.

The procedure of AHE measurement takes into account:

(a) a calibration by the sealed tungsten lamp,
(b) regular cross-check of accuracy powering a platinum wire resistor inside the reactor (which can be used as calibration resistance inside the reactor),
(c) measurements powering the active wires (CN).

8. Conclusions

Based on calibrations with the tungsten lamp at 10–120 W, the mean calibration constant in the power range of immediate interest (90–110W) was 0.200 ± 0.010°C/W. The calibration constant when powering a Constantan wire comprised of 14 knots (8 loops), has been on average 0.242± 0.010°C/W. This value was obtained at 2 bar of deuterium. When the pressure is reduced to about 0.1 bar a significant increase of the AHE was measured. A few days before the presentation of this paper, we activated a second wire inside the reactor comprised of 32 knots with four wire

Figure 7. Photo of the air flow calorimeter with both reactor (*top*) and calibration lamp (*bottom*).

loops each. Preliminary measurements confirm AHE values obtained in previous experiments with same knot design. Experiments previously reported at ICCF21 gave stable excess power of 6–7 W with an input power of 100–120 W. With the new knot design the excess reaches 20–25 W at similar input power.

Taking into consideration:

- current path in the Capuchin knot,
- size of the knot (few mm),
- large magnetism" of the wire induced by the multilayer coating of FeOx and SrO,
- "boil-off" of electrons at the inner and hotter area of the knot.

We speculate that, when in operation, a magnetically confined plasma may arise inside the knot.

Indeed, the "boil-off" of electrons, due to the low work function of the coating, may lead to a localized non-neutral plasma. The interaction of this non-neutral plasma with the nanostructures on the wires and sheaths will be object of

Figure 8. Photo of the reactor including a safety cage.

Table 1. The most significant measurements are summarized in this table (CN, 8N stands for Constantan wire with eight knots; 4N stands for Constantan wire with four knots).

Date DMY, Tot. time meas. (ks, kilo-second)	Type of meas.	P_w(W) V(V); I(A)	T_{in} fan (°C)	T_{out} fan (°C)	T_{SS}, int. React. (°C)	T_{ext} react (°C)	React. Gas Press. (bar)	$\Delta T/P_{in}$ (°C/W); Excess P_w (W)	Note
250918 90 ks	Calib. W lamp	0	21.2	22.4	22.9	22.3	Dynamic vacuum <0.001		Offset due to the fan.
260918 50 ks	Calib. W lamp	70.55	21.42	35.02	43.6	42.9	Dynamic vacuum < 0.001	0.1928	
6 ks	Calib. W lamp	50	21.51	32.15	38.6	37.8	Dynamic vacuum <0.001	0.2128	
7 ks	Calib. W lamp	30.2	22.2	28.5	32.8	32.4	Dynamic vacuum <0.001	0.2086	
7 ks	Calib. W lamp	10*	21.7	24.49	26.6	26.4	Dynamic vacuum <0.001	0.279	
11 ks	Calib. W lamp	120	24.6	48.76	61.7	61.0	Dynamic vacuum <0.001	0.2013	
270918 61.6 ks	Calib. W lamp	110.3	22.42	44.52	57	56	Dynamic vacuum < 0.001	0.2003	**Calibr. Extrap.at 100W=0.20**
7.5 ks	Calib. W lamp	90	22.8	40.2	51.5	50.3	Dynamic vacuum < 0.001	0.193	
7 ks	CN, 8N	50.6; -41.41, -1.23	22.6	32.6	291.7	110.7	Air flux, 0.1	0.198	Cleaning 8N
61 ks	Pt	65.6; -58.95 -1.11	21.9	35.67	230.9	99.6	Air flux, 0.1	0.2099 +3W	Calib. Extr. at 60W=0.20
011018 230 ks	CN 8N	91.2 -53.2 -1.71	23.2	42.5	409.9	170.4	D_2 0.92	0.2116 +10W	First loading D_2
021018 80 ks	CN 8N	98.5 -54.8 -1.796	22.7	44.0	426.7	174.4	D_2, 0.90	0.2162 +6.5 W	
031018 56 ks	CN, 8N	93.1 -53.78 -1.73	22.3	44.9	379.1	162	Xe=D_2 0.738	0.2427 +19.9W (cal.0.20)	At RT P =0.45 bar

031018 12 ks	CN 8N	100.6 - 56.0 - 1.795	23.7	47.5	397.7	170.6	Xe=D_2 0.744	0.2365 +18.4W (cal=0.20)	
031018 5ks	CN 8N	100.3 - 55.95 - 1.793	23.2	47.9	400.1	169.6	Xe=D2 0.43	0.2462 +23.5W (cal=0.20)	Press. reduced
031018 6 ks	CN 8N	100.7 - 56.25 - 1.79	23.5	48.1	416.2	169.7	Xe=D_2 0.24	0.2443 +22.3W (cal=0.20)	Press. reduced
031018 8.5 ks	CN 8N	100.5 - 55.47 - 1.811	24.3	48.8	443.4	172.3	Xe=D_2 0.107	0.2438 +22.5W (cal=0.20)	Press. reduced
041018 56 ks	CN 8N	101 - 55.7 - 1.81	23.38	47.92	433.8	171.4	Xe=D_2 0.100	0.2430 +21.7W (cal=0.20)	Counter electr.at GND
041018 9ks	CN 4N	91.2 - 52.8 - 1.727	24.1	45.9	278	187	D_2 3.23	0.239 +17.8W	First time D2 on 4N
041018 6ks	CN 4N	91.05 - 53.3 - 1.708	24.08	46.27	333	191	D_2 0.26	0.2437 +19.9W	Press. reduced

*Larger value of $\Delta T/P_{\text{in}}$ due to the offset arising from the fan self-heating.

deep investigations and reported at ICCF22.

Acknowledgments

The experimental work described in this paper was carried out mainly at INFN-LNF; some key trials were conducted at the premises of a LENR Laboratory located in a metallurgical company in northeast Italy, which has also financially helped our group since 2011. SIGI (Società Italiana di Guaine Isolanti) designed and produced innovative/unconventional types of glassy sheaths in a joint collaboration with our Group, the Favier Company (France side

of SIGI) and the aforementioned metallurgical company. Starting in October 2017, an important political group in Italy (Lega Nord) pushed the president of INFN to allow the continuation of F. Celani's experiments in the Frascati Laboratory, although he had reached the age-limit of retirement. The key people involved were Francesco Malagoli, Filippo Panini, Paolo Varini (all from Modena City). All of them have followed LENR studies since 2010, as part of their strategic political program on environmental protection and pollution reduction. Antonino Cataldo and Stefano Bellucci (NEXT collaboration) performed SEM and EDX analysis at INFN-LNF. Some of the funding to perform experiments was supplied by IFA (an Italian organization working on water and energy). We thank the Referees because useful suggestions given to improve our paper. We are indebted to Eng. Jed Rothwell for carefully reading our paper and largely improving our sentences about English Language.

References

[1] S. Romanowski, W. M. Bartczak and R. Wesołkowski, Density functional calculations of the hydrogen adsorption on transition metals and their alloys an application to catalysis, *Langmuir* **15** (18) (1999) 5773.

[2] W. Brückner, S. Baunack, G. Reiss, G. Leitner and T. Knuth, Oxidation behaviour of Cu–Ni(Mn) (constantan) films, *Thin Solid Films* **258** (12) (1995) 252.

[3] Francesco Celani, E.F. Marano, A. Spallone, A. Nuvoli, B. Ortenzi, S. Pella, E. Righi, G. Trenta, F. Micciulla, S. Bellucci, S. Bartalucci, M. Nakamura, E. Purchi, G. Zangari, S. Cupellini, A. Mancini, F. Maggiore and A. Ovidi, Experimental results on sub-micro structured Cu–Ni alloys under high temperatures hydrogen/deuterium interactions, *Chem. Materials Res.* **3** (3) (2013) 27–56.

[4] F. Celani, A. Spallone, B. Ortenzi, S. Pella, E. Purchi, F. Santandrea, S. Fiorilla, A. Nuvoli, M. Nakamura, P. Cirilli, P. Boccanera and L. Notargiacomo, Observation of macroscopic current and thermal anomalies, at high temperatures, by hetero-structures in thin and long constantan wires under H_2 gas, *J. Condensed Matter Nucl. Sci.* **19** (2016) 29–45.

[5] F. Celani, G. Vassallo, E. Purchi, S. Fiorilla, L. Notargiacomo, C. Lorenzetti, A. Calaon, B. Ortenzi, A. Spallone, M. Nakamura, A. Nuvoli, P. Cirilli, P. Boccanera and S. Pella, Improved stability and performance of surface-modified Constantan wires, by chemical additions and unconventional geometrical structures, *J. Condensed Matter Nucl. S*ci. **27** (2018) 1–13.

[6] F. Celani, C. Lorenzetti, B. Ortensi, A. Spallone and E. Purchi, Steps to identify main parameters for AHE generation in sub-micrometric materials: measurements by isoperibolic and air-flow calorimetry, *J Condensed Matter Nucl Sci.* **29** (2019) 52–74.

J. Condensed Matter Nucl. Sci. 30 (2020) 36–43

Research Article

Beyond Hydrogen Loading

Gianni Albertini*

Università Politecnica delle Marche (UNIVPM), Via Brecce Bianche, 60131 Ancona, Italy

Massimo Rogante

Rogante Engineering Office, Contrada San Michele 61, 62012 Civitanova Marche, Italy

Abstract

While experimental and technological attention is focused on the operational methods for hydrogen loading in metals and on the observed anomalies with respect to well-established rules, we aim to remark that these methods and these consequences can be seen as a part of a more general problem. In fact, most of the experiments and deductions of material sciences are based on the assumption that space–time is flat and isotropic (Minkowskian). After discarding this assumption, a theory of Deformed Space Time (DST) was developed in the last decades. Following this theory, experimental results were obtained which are not predicted by the Standard Model. The DST-theory concerns the fundamental interactions and in particular the nuclear ones, that can play the main role in the observed anomalies. In order to consider a nuclear reaction as a DST-reaction, four main phenomenological features were deduced: occurrence of an energy threshold; change of atomic weight; absence of gamma radiation; anisotropic emission of nuclear particles in intense beams having a very short life span. From the experimental point of view, rather than looking for fortuitous events that produce the conditions for DST-reactions, more systematic research can be undertaken by following the above reported four general rules. In particular, the occurrence of thresholds can correspond to a latency time, required to reach the energy density necessary to deform space–time. The absence of gamma radiation cannot be considered as a sign that nuclear reactions are not present; in fact, in absence of detected gamma radiation, elements were found which were not present before the reaction. The nuclear emissions, which are anisotropic and impulsive, can be difficult to detect with the traditional methods, thus inducing incertitude on the occurring reactions. Finally, a rapid variation of energy density is an experimental common factor of DST-reactions. Thus, the DST-theory can be the leading theory in the design of the experiment and in the interpretation of its experimental results.
 ISSN 2227-3123

Keywords: Deformed space–time theory (DST-theory), DST reactions, Gamma emissions, Hydrogen/deuterium loading, Local Lorentz invariance breakdown, Low energy nuclear reactions, Neutron emission, Ultrasounds

Foreword

While reading this contribution, we invite you to free your mind from previous assumptions and to imagine a world different from the one our experience and the experience of past generations push us to consider as real.

*Corresponding author. E-mail: gialbe50@gmail.com.

© 2020 ISCMNS. All rights reserved. ISSN 2227-3123

In fact, the most of our knowledge is based on the inputs coming from our instruments and from sight, hearing, touch, taste, smell: their functioning is based on the electromagnetic interaction. Thus, the world we know is mainly the world of electromagnetic interaction: the space is isotropic, homogeneous and flat while the time flows at a rate that, until the end of the XIX century, was assumed to be constant.

Imagine that, beside this world, other worlds exist where the opposite directions are not specular (this is already accepted in the Standard Model for the weak nuclear interaction) and/or space–time is not flat and/or time flows at different rates (as Einstein relativity says) with respect to our detection instruments; each of the four fundamental interactions acts in a different world. No matter that the electromagnetic and the weak nuclear ones are the same interaction, as all the interactions are tried to be seen as one sole interaction in the Great Unification Theory! In the range of energy where we live, four interactions are acting and each one gets its own world [a].

The question if the different worlds are in the same position at the same time can be without answer, as different space–times occur.

A neutron can live in these four different worlds and, while free to wander in the world of an interaction, it can be confined in the nucleus in another interaction. If an appropriate energy concentration can deform the world of the latter interaction in such a way as to make it somehow similar to the first, "deformed" world of the former, the neutron can escape from the nucleus without gamma emission, as the gamma energy is used to keep the space–time deformed; so, other neutrons in the surrounding can escape and an intense beam is emitted.

These emissions are not isotropic in space nor constant in time for us, as they were produced in a space–time that is deformed with respect to ours.

Thus, while in the traditional nuclear reactions a large amount of energy is needed to overcome the energy barrier keeping the nucleon confined and some gamma energy is emitted, in a Deformed Space–Time (DST) reaction the amount of energy can be lower and no gamma emission is observed.

As the reactions occur in a deformed space–time, in our world they are not-isotropic and not-constant in time, so that a violation of the Local Lorentz Invariance (LLI) is evident, as this invariance imposes an isotropic space and a flat (Minkowskian) space–time.

In the same way, the violation of LLI occurs in the electron emissions from ^{60}Co: in fact, parity is well known not to be conserved due to the weak nuclear interaction.

1. Introduction

According to what is now called the DST-theory, different metric parameters correspond to the different fundamental interaction (Mignani Metrics) [1,2].

These parameters were deduced from the experimental data concerning the leptonic decay of the meson K_{0S}[3,4] (weak interaction), pion pair production [5] (strong interaction), superluminal waves in conducting waveguides [6–10] (electromagnetic interaction) and clock rates at different height [11] (gravitational interaction).

These parameters are not constant but depend on energy, thus allowing different deformation of the space–time to occur at different energy.

The relationship between the time parameter "b_{T}", the spatial parameters "b_X", "b_Y" and "b_Z" and the space–time deformation is obtained by considering the generalized space–time distance "ds":

$$\mathrm{d}s^2 = b_{\mathrm{T}}^2 c^2 \mathrm{d}t^2 - b_X^2\,\mathrm{d}x^2 - b_Y^2\,\mathrm{d}y^2 - b_Z^2\,\mathrm{d}z^2$$

[a] We remark that we are not dealing the question of the so called "Parallel Universes". We are dealing the problem of the "Multimetrics", concerning the occurrence of different metric parameters of the interactions operating in the same phenomenon.

(*ct, x, y, z* being the coordinates of a point in the space–time and c the light speed in vacuum in a not-deformed space–time).

The deformation of one space–time with respect to another can be evaluated by a deformation coefficient, which is the ratio between the two corresponding values of ds^2.

The not-deformed condition (Minkowsky space–time) corresponds to all squared parameters equal to 1. The corresponding deformation coefficient is 1.

At increasing energy, four different thresholds occur for the four interactions, as shown in Fig. 1.

To the electromagnetic interaction, space–time is deformed *below* the threshold of 4.5 ± 0.2 μeV, due to the space parameters; the deformation coefficient is less than 1 and increases with energy until attaining the value 1 at the threshold.

To the gravitational interaction, the space–time is deformed *above* the threshold of 20.2 ± 0.1 μeV, due to the time parameter, and the deformation coefficient increases at higher energy. (The behaviour of space parameters could not be deduced from the behaviour of clocks at different heights.)

To the weak nuclear (or leptonic) interaction, the space–time is deformed *below* the threshold of 180.4 ± 0.2 GeV, due to the space parameters and the deformation coefficient reaches the value 1 coming from lower values.

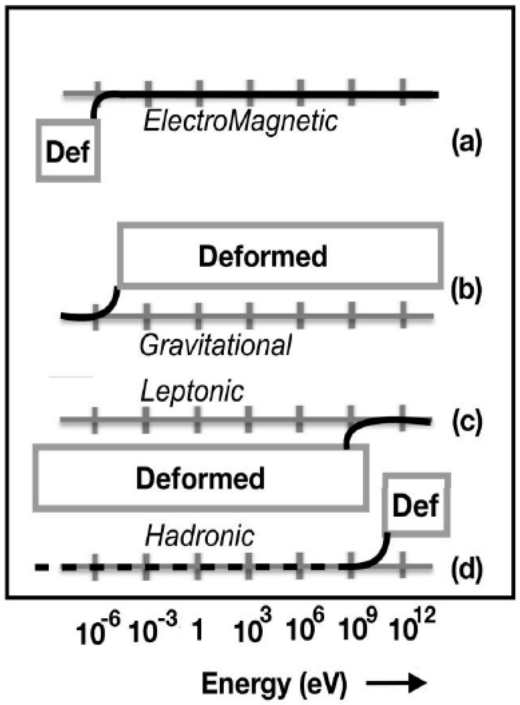

Figure 1. Metric deformation coefficients of the four fundamental interactions as functions of energy (a pictorial representation). The grey lines correspond to the Minkowsky space–time (all space and time parameters are equal to 1 and the deformation coefficient is 1). (a) *Electromagnetic interaction*: space–time is deformed below the threshold of 4.5 μeV, due to the space parameters. (b) *Gravitational interaction*: space–time is deformed above the threshold of 20 μeV, due to the time parameter. (c) *Weak nuclear interaction*: space–time is deformed below the threshold of 180 GeV, due to the space parameters. (d) *Strong nuclear interaction*: space–time is deformed above the threshold of 367.5 GeV, due to one space parameter and the time parameter. Below this threshold, however, space is not isotropic (*dashed black line*).

To the strong nuclear (or hadronic) interaction, the space–time is deformed *above* the threshold of 367.5 ± 0.4 GeV, due to two parameters: one of space and another of time; the deformation coefficient is higher for higher energy. Below this threshold, however, although the metric parameters are constant, the space is not isotropic.

In this framework, the space–time of electromagnetic interaction is Minkowskian in the range of energy in which we usually operate (i.e. greater than 5 μeV)**.**

2. The Core Question

Using the above-reported thresholds of energy in a technological problem is not easy. However, the corresponding thresholds of energy density, which is easier to evaluate in material science, were evaluated in a recent paper [12].

To this aim, the volume where this amount of energy is stored when a DST-reaction takes place was considered. In fact, two classes of experiments, one in liquid material and the other in solids, put in evidence that the micro-reactors where the reactions occur are in any case of similar size: i.e. some microns.

In the case of liquids, the application of ultrasound, either to pure distilled water [13–15] or to water solutions [16], produced neutron emissions and modification of the elemental composition only if the sonication bubbles were a few microns in size.

People working in the field of ultrasound were sceptical about these results, as they never detected similar effects in their many-years of experience. However, a report [17] describes transmutations and particle emissions after sonication of pure water. In this case, no explanation was given in terms of DST-reactions, which presumably were unknown to the author.

In the case of solids, the application of ultrasound to four samples, two of sintered Ferrite and two of carbon hardened steel, resulted in the emission of neutrons and the presence of elements that were not present in the corresponding original samples [18] .

From electron microscopy images and elemental analysis by X-ray energy-dispersion spectra, it was deduced [19,20] that a nuclear reaction occurred inside some of the cavities already present in the material. The dimensions of these micro-reactors (Ridolfi cavities) were a few microns, similar to the sonication bubbles.

In order to slow down the particle emissions, the compression/expansion cycles induced by the ultrasound in the materials with a period of 50 μs were replaced by five slower compression/expansion cycles of mechanical presses [21,22] on the order of 10^2–10^3 s. Each of them was composed of a pre-load of 60 s at 300 N, a compression phase at fixed strain rate of 1, 2, 3, 4 or 5 micron/s respectively up to a load of 160 kN, and a fast stress release phase from 160 kN to 300 N of about 10 s. The rationale of this change is the same used in the classical nuclear reactors, where the fast processes of an atomic bomb are slowed down to use them in a less dangerous and more controlled way.

Also at this slower rate, nuclear particle emissions (alpha particle [21,22] or neutron [23] emissions) were detected.

Although the mechanical cycles were slowed down, we presume that the single reaction was caused by a sudden and catastrophic local variation of energy concentration, analogous to the case of ultrasound. In the studies making use of ultrasounds in liquids, a sudden catastrophic energy concentration was assumed to be created by the implosion of the bubbles. Due to its radius, which is very small with respect to the ultrasound wavelength, each bubble is subjected to a locally isotropic pressure during sonication. The reduction of the radius to almost zero occurs at the very high speed of a shock wave: thus, in a very short time the energy of the bubble was concentrated into a volume almost reduced to zero.

The conditions of high energy concentration in the space and high variation of energy density in the time were thus produced.

In a similar way, when ultrasound was applied to solids [18–20], the radius of the Ridolfi cavities was very small with respect to the ultrasound wavelength, so that an isotropic pressure acted on each cavity and compressed its internal part down, with consequent high variation of energy density in a short time.

Further support to this assumption came from two kinds of natural rocks, green Luserna granite and Carrara marble, which were compressed until they ruptured [24]. Neutron emissions were detected in granite, characterised by a brittle sudden fracture, while no intensity higher than the background noise was registered in marble, which is characterised by a slow ductile rupture.

The neutron emissions were not isotropic. In fact, they were in a very intense neutron beam detectable only in some directions.

The anisotropy was more deeply studied in an AISI 304 cylinder kept in the vertical position inside a cylindrical Teflon calorimeter, surrounded by 16 CR39AB neutron detectors [25–27]. The sample was irradiated by 20 MHz ultrasound with a maximum power of 2 kW.

Also in this case, neutron emissions were recorded: their intensity was very intense along two opposite horizontal directions and absent in the two horizontal opposite directions perpendicular to them. No gamma radiation above background was detected.

The geometry of this experiment was the starting point for the realisation of a reactor able to transform liquid Mercury into solid material [28–30]. This material contained elements not present in the original sample nor in the parts of the experimental apparatus in contact with it. Among the produced elements, rare earths were also found [30].

3. Discussion

In the above-reported experiments, low-energy nuclear reactions are described which are based on DST-reactions.

Different materials were used: pure water [13–15], water solutions [16], natural rocks like marble and granite [24], technological metals like ferrite and steels [18–23], a liquid metal, i.e. mercury [28–30].

Also, different techniques were applied to induce the adequate energy concentration inside the materials. A question arises: what are the main features we can extract from all these experiments, so that we can recognize a reaction as a DST-reaction?

The occurrence of one or more thresholds in energy is the first characteristic. In order to transform a flat space–time into a deformed one, or vice versa, an adequate energy density must be achieved. This value not only depends on the energy threshold, but also on the occurrence of suitable sites, having the right size, to act as micro-reactors [12].

There is a reason why a larger site with a larger amount of energy, thus having the same density, or with smaller density, thus containing the same energy, is not suitable. This can be determined by considering the time. As the space–time – not only the space – is the critical parameter, the density of energy in time, or better the variation of energy per unit time, is also important.

We hypothesise that a “coherence time interval” must be considered, for the effective variation of energy. Thus, a larger distance corresponds to a time too long to consider all the energy as a sole amount of energy. However, no measurement has been performed to better define this time interval.

From a technological point of view, reaching the required energy density means that a latency time [31] can be observed between the input of energy and the start of the reaction. From the macroscopic point of view, reaching this density corresponds to the beginning of the reaction. Conversely, the sudden variation of energy – not the amount of energy – is responsible of the single reaction inside the single micro-reactor.

Nuclear DST-reactions are of great interest to shed light on the large number of experiments dedicated to LENRs [31]. However, DST-reactions concern all interactions, not only nuclear ones.

A further characteristic of DST-reactions is that, although variations of atomic weights and/or nuclear particle emission are detected, no gamma emission is detected. This fact is explained if the energy of the gamma radiation is adsorbed to keep the space–time deformed.

This point is of great importance for the people working in the field of LENRs, as one of the main reasons why sceptics find it difficult to accept these nuclear reactions is the absence of gamma radiation.

In DST-reactions, the emissions of nuclear particles are very intense, anisotropic and impulsive beams. Their detection needs precautions. In fact, a large solid angle must be explored to include the few directions of emission. In addition, most traditional detectors and their electronics may count a short-living signal of many particles as one only particle, which can be included in the statistic fluctuation of the background, or even cancel it out as a noise, due to its short duration.

These facts make the evaluation of the mass balance of the studied reactions difficult.

In this framework, a leading guide for future experiments of hydrogen loading is that the different methodologies will get an "a priori" planning or an "a posteriori" explanation considering them as different methods to realise the conditions suitable for DST-reactions.

Those difficulties that made LENRs difficult to accept by the scientific community – mainly: absence of gamma radiation; energy input too low to realise nuclear reactions; mass balance not possible – are resolved and, on the contrary, are good indicators for considering the occurrence of DST-reactions.

4. Conclusions

Hydrogen loading in a suitable way can be one of the methods to create the conditions necessary to induce nuclear DST-reactions. There are some common features to recognize these reactions and, more usefully from the technological point of view, to induce them.

The most important condition is to obtain the right energy density in the space and the right variation of energy over time. However, these quantities are concerned with the microscopic scale while the experimenter operates at a macroscopic scale. Thus, different technologies must be tested and analysed to obtain these conditions.

The knowledge of these suitable conditions, and of the experimental evidence already obtained, is a reference point for the design of future experiments and for understanding the past and future experimental results.

As an example, the importance of deuterium has been discussed for a long time, and some analogy with the well-known fusion of hydrogen has been searched for. If one considers the alpha emissions obtained in DST-reactions, the occurrence of helium can rather be a consequence of alpha emission than the product of traditional fusion. On the other hand, the active role of deuterium, as well as of hydrogen, should be analysed in terms of energy accumulated, for instance in deforming the crystal lattice, and in abrupt energy release, for instance when the crystal lattice collapses locally.

In a similar way, the DST-theory can be the leading theory for the interpretation of experimental results in the other cases.

References

[1] F. Cardone and R. Mignani (Eds.), *Energy and Geometry*, World Scientific, Singapore, 2004.

[2] F. Cardone and R. Mignani (Eds.), Deformed Space–time, Springer, Dordrecht, The Netherlands. ISBN 978-1-4020-6282-7 (HB) ISBN 978-1-4020-6283-4 (e-book) (2007).

[3] S.H. Aronson, G.J. Bock, H.-Y. Chang and E. Fishbach, Energy dependence of the fundamental parameters of the K0− K0 system, II. Theoretical formalism, *Phys. Rev*. D **28** (1983) 495.

[4] N. Grossman, K. Heller, C. James, M. Shupe, K. Thorne, P. Border, M.J. Longo, A. Beretvas, A. Caracappa, T. Devlin, H. T. Diehl, U. Joshi, K. Krueger, P. C. Petersen, S. Teige and G.B. Thomson, Measurement of the lifetime of K0S mesons in the momentum range 100–350 GeV/c, *Phys. Rev. Lett.* **59** (1987) 18.

[5] UA1 Collaboration Bose–Einstein Correlations in pp Interactions at $\sqrt{s}$= 0.2 to 0.9 TeV, *Phys. Lett*. B **226** (1989) 410. DOI: 10.1016/0370-2693(89)91221-5.

[6] A. Enders and G. Nimtz, On superluminal barrier traversal, *J. Phys. I* (France) **2** (1992) 1693–1698. DOI: 10.1051/jp1:1992236.

[7] A. Enders and G. Nimtz, Zero-time tunneling of evanescent mode packets, *J. Phys. I* (France) **3** (1993) 1089–1092. DOI: 10.1051/jp1:1993257.
[8] A. Enders and G. Nimtz, Evanescent-mode propagation and quantum tunnelling, *Phys. Rev.* E **48** (1993) 632. DOI:https://doi.org/10.1103/PhysRevE.48.632.
[9] A. Ranfagni, D. Mugnai, P. Fabeni and G. P. Pazzi, Delay-time measurements in narrowed waveguides as a test of tunnelling, *Appl. Phys. Lett.* **58** (1998) 774. DOI: https://doi.org/10.1063/1.104544.
[10] A. Ranfagni, P. Fabeni, G. P. Pazzi and D. Mugnai, Anomalous pulse delay in microwave propagation: A plausible connection to the tunneling time, *Phys. Rev*. E **48** (1993) 1453, DOI:https://doi.org/10.1103/PhysRevE.48.1453.
[11] C. Alley, Proper time experiments in gravitational fields with atomic clocks, aircraft, and laser light pulses, in P. Meystre and M.O. Scully (Eds.), *Quantum Optics, Experimental Gravitation, and Measurement Theory, Proc. of the NATO Advanced Study Institute on Quantum Optics and Experimental General Relativity*. August 1981, Bad Windsheim, Germany, NATO Science Series: B, Vol. 94, pp. 363–427 Plenum Press, New York, 5 (1983).
[12] F. Cardone, V. Calbucci and G. Albertini, Deformed space time of the piezonuclear emissions, *Mod. Phys. Lett*. B **28** (2) (2014) 1450012.
[13] F. Cardone and R. Mignani, Possible evidence for transformation of chemical elements in cavitated water, *Int. J. Mod. Phys*. B **17** (1995) 307.
[14] F. Cardone, R. Mignani, W. Perconti, E. Pessa and G. Spera, Possible evidence for production of an artificial radionuclide in cavitated water, *J. Radioanal. Nucl. Chem.* **265** (2005) 151.
[15] F. Cardone, R. Mignani, W. Perconti, E. Pessa and G. Spera, Nucleosynthesis of an artificial radionuclide by cavitation, *Gravitation and Cosmology* **11** (1–2) (2005) 41–42.
[16] F. Cardone, G. Cherubini, R. Mignani, W. Perconti, A. Petrucci, F. Rosetto and G. Spera, Neutrons from Piezonuclear Reactions, *Annales de la Fondation Louis de Broglie* **34** (2009) 138.
[17] Mark Leclair, Water alchemy: harnessing the power of cavitation reentrant jets, *Pulse Magazine*, Spring 2014, Issue 2 (2014) 6–11.
[18] F. Cardone, R. Mignani, M. Monti, A. Petrucci and V. Sala, Piezonuclear reactions from iron, *Mod. Phys. Lett.* A **27** (18) (2012) 50102.
[19] F. Ridolfi, F. Cardone and G. Albertini, Ultrasonic damages in iron, *J. Adv. Phys.* **2** (4) (2013) 40–44.
[20] G. Albertini, F. Cardone, M. Lammardo, A. Petrucci, F. Ridolfi, A. Rosada, V. Sala and E. Santoro, Atomic and isotopic changes induced by ultrasounds in iron, *J. Radioanal. Nucl. Chem.* **304** (2) (2015) 955–963.
[21] F. Cardone, V. Calbucci and G. Albertini Possible evidence of Piezonuclear alpha emission, *J. Adv. Phys*. **2** (1) (2013) 20-24(5), 2168-1996/2013/2/001/005 – doi: http://dx.doi.org/10.1166/jap.2013.1029.
[22] G. Albertini, V. Calbucci, F. Cardone, G. Fattorini, R. Mignani, A. Petrucci, F. Ridolfi and A. Rotili, Evidence of alpha emission from compressed steel bars, *Int. Mod. Phys.* B **27** (23) (2013) 1350124. DOI: 10.1142/S0217979213501245.
[23] G. Albertini, V. Calbucci and F. Cardone, Statistics of piezonuclear emissions: early results, *Mod. Phys. Lett*. B.**28** (5) (2014) 1450036. DOI: 10.1142/S0217984914500365.
[24] F. Cardone, A. Carpinteri and G. Lacidogna, Piezonuclear neutrons from fracturing of inert solids, *Phys. Lett*. A **373** (2009) 4158–4163.
[25] A. Petrucci, A. Rosada and E. Santoro, Asymmetric neutron emissions from sonicated steel, *Mod. Phys. Lett*. B **29** (2015) 1550067. https://doi.org/10.1142/S0217984915500670.
[26] F. Cardone, G. Cherubini, M. Lammardo, R. Mignani, A. Petrucci, A. Rosada, V. Sala and E. Santoro, Violation of Local Lorentz Invariance for deformed space–time neutron emission, *Euro. Phys. J.* –Plus **130**, (2015) 55.
[27] A. Petrucci and A. Rosada, Ultrasonic neutron emission, *J. Adv. Phys*. **5** (2016) 63–68.
[28] F. Cardone,G. Albertini, D. Bassani, G. Cherubini, E. Guerriero, R. Mignani, M. Monti, A. Petrucci, F. Ridolfi, A. Rosada, F. Rosetto, V. Sala, E. Santoro and G. Spera, Nuclear metamorphosis in mercury, *Int. J. Mod. Phys*. B **29** (2015) 1550239. ©World Scientific. DOI: 10.1142/S0217979215502392.
[29] F. Cardone,G. Albertini, D. Bassani, G. Cherubini, E. Guerriero, R. Mignani, M. Monti, A. Petrucci, F. Ridolfi, A. Rosada, F. Rosetto, V. Sala, E. Santoro and G. Spera, Deformed space–time transformations in mercury, *Int. J. Mod. Phys.* B **31** (2017) 1750168. DOI: 10.1142/S0217979217501685.
[30] F. Cardone, G. Albertini, D. Bassani, G. Cherubini, E. Guerriero, R. Mignani, M. Monti, A. Petrucci, F. Ridolfi, A. Rosada,

F. Rosetto, V. Sala, E. Santoro and G. Spera, Nuclear metamorphosis in mercury: the rare earths production, *J. Condensed Matter Nucl. Sci.* **27** (2018) 1.

[31] G. Albertini and D. Bassani, Deformed space–time reactions and their phenomenology, *Phys. J.* **1** (3) (2015) 382–387.

J. Condensed Matter Nucl. Sci. 30 (2020) 44–65

Research Article

Deuteron Plasmas Driven to Neutrality and ^{4}He

Roger Sherman Stringham*

Firstgate, 4124 Kapuna Rd., Kauai, HI, 96754, USA

Abstract

This paper discusses Radio Frequency (RF) applied to cavitating D_2O, resulting in jet plasma implantation of charged separated electrons and a deuteron-compressed plasma pulse; these interactions involved hot charged particles at an effective temperature of 10^4 K in a sub-picosecond time frame A. Free electrons were focused on clustered deuterons that compressed the deuterons like a spherical piston, squeezing a Meso-Cluster (MC) of deuterons. The compressed clusters were different from the deuterium clusters used by A. Takahashi. A reaction pathway similar to muon fusion was observed. The RF applied at a deuteron resonance, produced charge neutrality in the plasma's electromagnetic (EM) pathway where alpha production was observed. Each MC consisted of 2–100 deuterons. Here we will use 10 deuterons to describe the MC and its alpha production, within time frame A. The changing MC density, pressure, and temperature were critical to alpha production, within time frame A. The MC volume was about 10^{-39} m^3 and compression force was continuously applied to the MC located at the target foil (TF) surface. The heat transport was fast, and MCs were confined by electromagnetic fields (EM) tangent to the MC interface and motion of the neutralizing electrons. It is conjectured in this paper that the neutralizing plasma in time frame A produced a shockwave (SW) using a single electron to form a D atom that fused two deuterons in the MC to create an alpha. Before the fusion reaction, the surface target foil atoms were cavitating for an active period of 100 ns duration with each RF cavitation resonance cycle (see the main text in Fig 4). The physical basis for the conjectured deuteron fusion reaction consisted of a preliminary compression cycle due to the electromagnetic field applied to the deuteron MC for a few hundred femtoseconds, followed by a rapid expansion. The compression cycle produced an effective temperature sufficient to create an alpha particle from the compression of two deuterons. The expansion cycle produced a slight temperature drop, allowing a deuterium ion to recombine with a low energy electron. This produced an orbital electron capture in the MC, forming a deuterium atom that jumped a distance 60,000 times larger than the deuteron's ionic radius. It is conjectured that this impulse fused two deuterons in the MC into an alpha particle. The Mass Spectrometer (MS) measurements of collected gas samples produced by RF MHz cavitation in Ar-saturated H_2O or D_2O in a target foil lattice supported this conjecture. This conjecture was only a model, as other reaction pathways likely exist. Malcolm Fowler of McFarland Instrumentation Service (AIM) performed the MS analysis for He4 in the gas-phase RF reaction products. The analysis for tritium was done by Tom Claytor of High Mesa Tech (HMT). Pd TF were checked for any ^{4}He retained in the Pd lattice. Electron mobility and target foil crystal types (face centered or body centered) may play an important role in the location of ^{4}He in the lattice structure.
 ISSN 2227-3123

Keywords: Cavitation resonance, Deuterons, Free electrons, MC clustered radio frequency, Target foils, Time frame

*E-mail: Firstgate@earthlink.net.

© 2020 ISCMNS. All rights reserved. ISSN 2227-3123

1. Introduction

The author discovered archived target foils that had been run in 1994 at Los Alamos National Laboratory by applying 2 MHz of RF to the foils in argon-saturated deuterium oxide. The 1994 target foils were re-analyzed recently by a high sensitivity mass spectrometer (MS) for the presence of ^{4}He and compared to the old data reported previously [1]. The collected gas samples were contaminated but the target foils were not. This data was recovered from old 1994 files and showed a reaction pathway that involved the implantation of electrons and deuterons into the Meso-Custer (MC). It is commonly known that ^{4}He remains stable in the metal lattice of the target foils; recent sensitive mass spectrometer measurements reported $40 \times 10^{12} \pm 1$ ^{4}He atoms in the target foils from 1994. The background ^{4}He in the argon tank that was used in all experiments was measured at 0.200 ± 0.006 ppm.

The current gas samples were collected and measured with the assistance of Tom Claytor for tritium and Malcolm Fowler for ^{4}He. The new MS was sensitive to 0.1 ppm. A chemically assisted reaction pathway to nuclear products appears to be possible and reproducible. New ^{4}He data produced by several RF experiments in the megahertz range is introduced in this paper. The D+D $\rightarrow ^4$He reaction mechanism remains valid for the new gas phase studies by Malcolm Fowler, based on mass spectrometer data from collected gas-phase Ar/D_2O samples.

The current tentative measurements from the gas phase of RF experiments with Pd target foils show amounts of ^{4}He that are consistent with the 1994 measurements. The reaction mechanism appears to be the same, as suggested by the measured presence of D_2 and DOOD in the evolved gas [2]. This ^{4}He was found in the Ar gas phase of the RF reactor with the difference being a contribution from the Acrylic surface of the RF reactor and its ions measured in the RF reactor's Ar gas phase. In summary, the old data and new data suggest the same reaction mechanism is present in both data sets, supported by the mass spectrographic measurements of steady state D_2 and DOOD. The mass ratio of D_2 and DOOD was consistently found in all samples over the last 27 years and is an important marker, as the same ratio appears in isolated systems impervious to time and instrumentation.

2. Cavitation Measurements

The goal of cavitation is to produce an MC by compression of deuterons and implant them into a metal lattice, typically palladium. As shown in Fig 1, when RF between 0.02 and 2 MHz is applied to deuterium oxide saturated with argon, many bubbles are produced. Only a select few bubbles will be resonant and assist in the formation of MC. Those that are of the resonant size, will follow the red trace in Fig 1, rapidly increasing in size, followed by a rapid and violent adiabatic collapse of the resonant bubble. At this point, the resonant/dense bubble ruptures to produce observable sonoluminescence (SL) and forms a compressing jet plasma that implants electrons followed by deuterons into a nearby target foil (TF). ^{4}He is produced in the MC during the time frame A, as depicted in Fig 1. When the resonant (dense) bubble collapses, it is conjectured that the effective temperature reaches 10^4 K or higher, which is sufficient to produce ^{4}He from two deuterons. When the bubble collapses, the effective temperature declines slightly and allows the recombination of one deuteron with an electron, producing a recombination SW capable of igniting single or multiple alpha fusion events within time frame A.

It is of note that at higher RF frequencies, the craters observed on the surfaces of typical target foils are of a similar size (50 nm diameter). The amount of energy required to create the crater can be estimated by estimating the volume of the missing metal, or ejecta. The number of lattices in the ejecta can be estimated and the energy required to rupture a single lattice of the target foil can also be estimated ($\sim$21 eV). With this data, the implied energy released in the target foil can be computed and is typically 4×10^{-12} J or 25 MeV. This value is consistent with the D+D $\rightarrow ^4$He reaction pathway.

The RF system is different from often-studied resonant systems [3] in that cavitation power is input into the RF reactor producing 40 W at about 1.3 atm of Ar-saturated D_2O. Typically, SL is coupled to the RF oscillating power input, as energy from the collapsed bubble is focused on producing a continuously pulsing SL emission. This energy

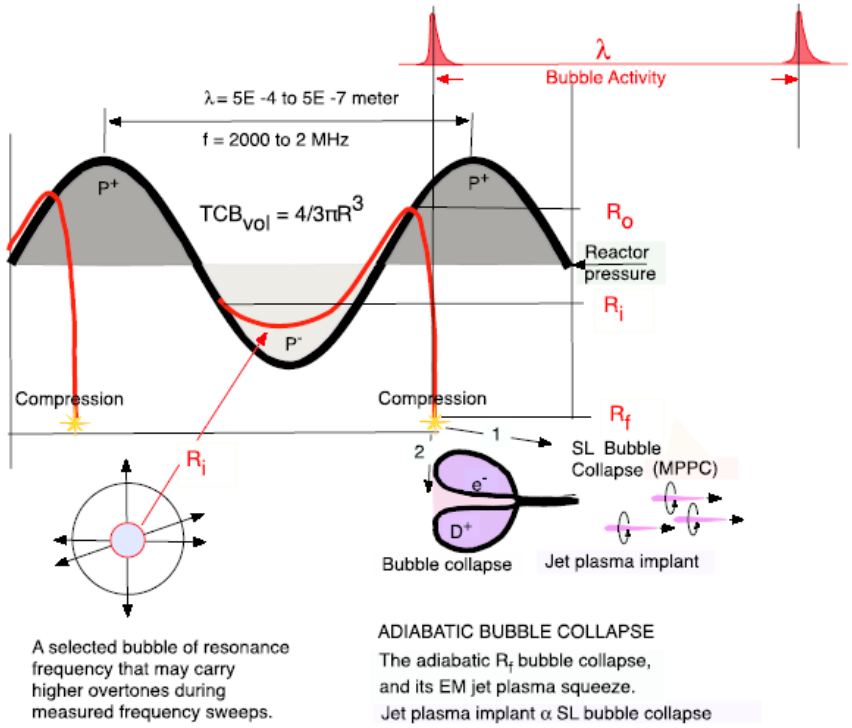

Figure 1. Acoustic input into water near a target foil, will resonate together to induce both observable and microscopic damage to surface and volume lattice of the TF. This damage can be catastrophic to the TF lattice depending on the power, frequency, and time [3]. The violent collapse of the bubble is less destructive as the frequency increases, as the bubble is reduced in size. The path of bubbles is shown in red, and its activity spread is shown also in red (see Fig. 3). During one cycle the measured SL emission is coupled to the jet plasma. The top arrow shows the extent of frequencies studied.

is dissipated in the lattice structure of the target foil (TF). The SL emission is monitored by a Multi-Pixel Photon Counter (MPPC) from Hamamatsu; the multi pixel devices show the system is in active mode about 10% of the time. The rest of the cycle time is spent in recovery mode for the next 10% active duty cycle. The active pulse, shown in red, is coupled to the general wave cycle. The system described above produces powerful acoustic output, and is focused on implantation of energy into the MC. The initial bubble, with radius R_{i}, begins in the negative pressure zone (P-negative) and gains momentum, reaching a maximum with bubble size, R_{o}; the bubble experiences a momentum-overshoot and is turned around in a recoil response, entering the high-pressure P^{+} zone as a high velocity pulse with SL emission and a high-energy jet plasma, as indicated by the yellow stars shown in Fig 1. The SL is coupled to the electromagnetically squeezed jet plasma and is accelerated by the jet plasma, leading to energy dissipation in the TF.

2.1. Acoustic measurements and beats

A Polyvinylidene Fluoride (PVDF) sensor strip was used in conjunction with a wide band pick-up using channel 2 of the TDS784D oscilloscope; the scope output shows the beat from the presence of another close-by frequency input that is about the same frequency as RF amplified input. The presence of the two signals may become a useful parameter to manipulate experimentally.

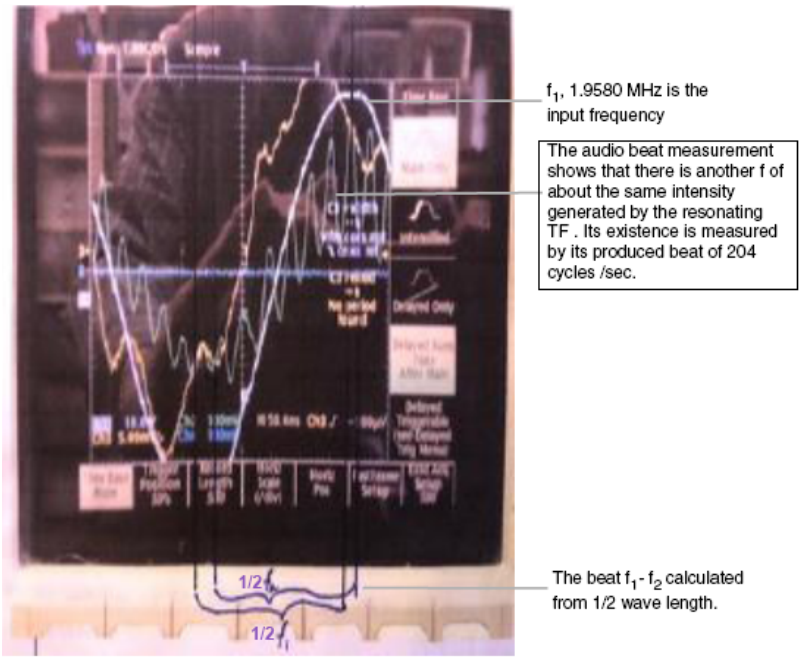

Figure 2. Shows a photo of the oscilloscope display during data collection in the RF running mode, with the RF input to the piezo antenna the half wave ($1/2f_1$) depicted in white, and the audio output from the PVDF sensor ($1/2f_2$) in green. The audio pick-up (green trace) represents the f_2 input frequency with a similar amplitude and the white trace (f_1,) represents the RF generator input of the target foil resonance. The two signals of different frequencies alternate between constructive and destructive interference, producing a beat frequency (f_b) that contains the alternating high and low maxima of the two interfering signals: $f_b = f_1 - f_2$. The MHz frequency of the RF input (f_1) minus the TF frequency of the second signal (f_2) is expected to be smaller than f_1 and is calculated as $f_1 - 204 = f_2$ cycles/s using the sums and differences equation. This calculation may be further complicated by the presence of overtones in f_1, as evidenced by the irregularities in the f_1 sine wave.

2.2. SL measurements

Figure 3 shows the MPPC SL output in ∼100 nm width SL emission pulses, shown in volts as blue peaks and they are coupled to the acoustic output (red trace); the scale is 1000 times the voltage output of the Hamamatsu MPPC. The scale is 50, 100, and 1600 pixels with wavelengths between 350 and 1000 nm. The reactor is a unique 1.5-inch diameter cylinder of machined polycarbonate, using a 0.0031-inch Pd wire as a TF and a cylindrical PZT piezo resonating at 0.63 MHz with Ar-saturated D_2O circulating through it. The reactor produced about 40 data graphs similar to the one shown in Fig. 3. The center of SL emission from the cylindrical PZT piezo was from the two 5 mm end openings, which made for a rather large emission source for the SL (9 mm). The SL measurements were taken in a 36× 36× 36 cm^3 dark box at three different MPPC distances within the box, using three different Hamamatsu MPPC devices while measuring their voltage output. The SL emission is proportional to the number of jet plasmas produced before implantation into the target foil wire lattice (see Fig. 1). The SL measuring emission surface has a spherical radius of d, and the largest sensing spherical surface area was 16 cm from the source (8 and 16 cm radius). The matrix of the time vs volts (4000 × 300) was adjusted a few nanoseconds to bring the voltage data into focus, showing the 100 ns periods on cavitation activity (blue).

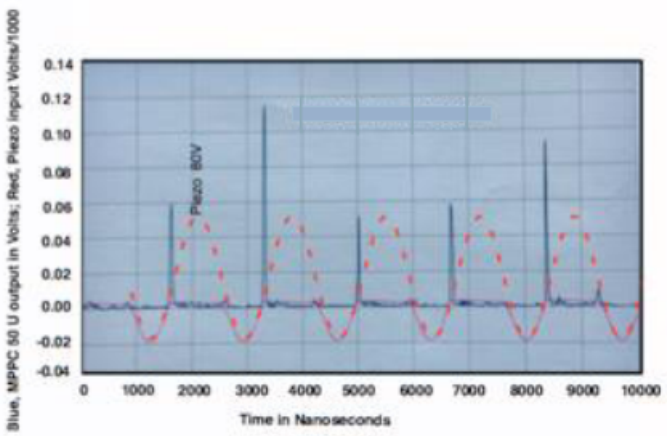

Figure 3. It is a typical data sheet from a reactor that circulated water through a cylindrical PZT piezo 17 mm long, 11 mm OD and 5 mm ID. This was done in a sealed light box, where SL emission was measured by MPPC devices donated by Hamamatsu. Through the center of the piezo is a sealed Pd wire; the acoustic energy was focused at the wire surface, as depicted by the red trace. The SL detection MPPC device was stimulated by a DC 80 V bias input. The SL output, depicted by the blue trace, was measured as a 100 nm half width voltage peak. The velocity of sound through D_2O was 1600 m/s, the distance from the inside diameter to the wire was 2 mm. The frequency was 1600 m/s over the distance of 2 cm resulting in 0.8 MHz frequency and the blue trace represented 100 nm of active resonance time.

The MPPC output is scaled to the number of photons counted times the proportional area of

$$\frac{\text{measuring sphere surface area}}{\text{MPPC detecting surface aera}}.$$

The bubble population that is involved in the sonofusion is applied to the surface of the oscillating TF wire and the piezo. It appears that the increase in the MHz range frequency that utilizes a much smaller bubble size maintains the same energetics and produces ^{4}He, while operating on a 10% duty cycle in the active mode as shown in Fig. 3 (also see λ in Fig. 1). It was found experimentally that operating at 20 kHz produced significant damage to the target foils, while operating at 2 MHz [4] produced less damage to the foils and motivated operating at higher frequencies.

When SL emission measurements are positive in the reactor and coupled to the input frequency, shown in Fig. 3 in red, plasma events like dissociation and recombination are occurring. The bubbles issued from both the piezo and the TF surfaces are involved in producing a deuterium ion and electron plasma for implantation in the MC [4]. The SL measurement shows the system is operating in a zone that is producing implanted MCs in the TF, and the implantation rate is proportional to the measured SL intensity as the two-bubble collapse products of SL and jet plasma, are found in every mass spectrometer study. There is also confirmation of SL products and jet plasma from recent mass spectroscopic work done by Malcolm Fowler of D_2 and DOOD steady state measurements [2].

2.3. System overview

Examining in more depth the relationships that makes MC implantation work, note that the SL emission for one cycle is proportional to the number of plasma jets that are shown in connection with a single SL pulse in Fig. 1. A collection of SL signals that show a sum of SL events are pulsed along a time line for 10,000 ns, as shown in Fig. 3. For one MC pulse starting in the gas phase in time frame A at $\sim$10,000 K, where $D_2^+ \rightarrow 2D^+ +$ e and the implanted jet plasma pulse are in a state of free mobile electrons; the free highly mobile electrons surround the almost stationary MC deuterons

and atoms of the TF lattice. The system is naturally driven by the neutralization resulting from the charge difference between the spherical electrostatically focused mobile electrons at the center of the immobile MC. There was seldom a $D^+ + e^- \rightarrow D$ recombination because of the high temperature. The time frame A and the mobility of the particles that make up the MC in the gas phase produced a total of approximately 10^{12} MC implantations per-second, producing approximately 40 W of anomalous power. Each MC is an active implant center; at each MC site, the deuterons within the MC are electrostatically squeezed with the center focus of the spherical cloud mobile free electrons, and this squeeze produces compression heating of MC deuterons. Additionally, an electromagnetic tangent field provides the surrounding containment of TF atoms that also squeezes the deuterons but does not promote recombination in the MC. The measured amount of ^{4}He is unexpected but is a result of an inefficient process.

The ultimate goal is to make this a more efficient process. In the given time frame A, the free electron mobility, points to a periodicity shadow in the unit cell that is occupied by an MC; during its TF confinement, the mobility drift of the target foil's relatively large atoms during MC containment is small. A deuteron cluster in the atom's unit cell interstitial space has a higher mass density than the target foil resulting in a static MC in time frame A. Basically, there is no real movement of atoms except the compression-producing electrons during the MC deuteron confinement. In the gas phase, the target foil lattice atoms remain in the same lattice space, exhibiting their shadow behavior in the gas phase during the time frame A. In reality, there are continuous changes of crystal structure during the heat-pulse compression, and structures such as BCC and FCC crystals are not clearcut on the atomic scale [4]. The activity of crystal changes has time factors for changes along with Brillioun effects [5].

3. Experimental

3.1. The RF reactor

The radio frequency system is a non-obvious extension of SF, where a replacement of the oscillator with an RF input to the 1.7 MHz piezo is now an antenna that is tuned to minimum RF reflection and maximum admittance with a standing wave ratio (SWR) of one, indicating 100% signal transmission. There are other tuning methods that can be utilized: oscilloscope voltage, the frequency resonance, the visual D_2O surface, and the oscilloscope overtones. Some new discoveries about the cavitating system have been made during this experimental campaign: (1) there is more than one vibrating surface and (2) the fundamental vibration may make some large contributions to the resonant bubble population via overtones.

Experimentally, RF interference was a major concern that accompanied all measurements made while the RF system was running. To minimize RF interference upon instrumentation, a duty cycle was introduced of 30 s on and 5 s off that provided an adequate time window for credible measurements of temperature; this feature was built into the calorimetry of both the RF mode and calibration mode (see Figs. 5–10).

Two years of RF practice runs with H_2O suggested that enough knowledge was in place to do controlled runs with D_2O. There was a completely different philosophy in the new RF rector. The reactor was no longer a small polycarbonate 50 g reactor with a 1 cm^3 of actively cavitating volume with 1 ml circulation rate of D_2O.

The new RF reactor was machined by Hans Huber from a 6-inch acrylic tube, having a 2-inch diameter with quarter-inch walls. A one-inch thick by 3-inch diameter disk top was provided, where all the utility and measuring pass-throughs were positioned, except for the RF input placed at the tube bottom with the RVDF audio pickup (see Fig. 4A). A 1/8-inch diameter copper cooling coil of 16 turns was submerged in the static D_2O. This coil moved fluid at a measured rate of $1\pm$ 0.02 ml/s (see Fig. 4B). The purpose was to remove heat, keeping the D_2O at a constant temperature that was reached after running about 1000 s. The water coolant flows from Cu coil # 1 through a closed loop to an equivalent second copper coil submerged in 3.5-liter coolant reservoir and circulates back to the D_2O coil #1 for another cooling cycle (see Fig. 4B). The pump is an FMI displacement pump moving H_2O coolant measured at a constant ml /s. The reactor measured heat DT_1 (the output of the coil minus the input of the coil) plus DT_2 heat

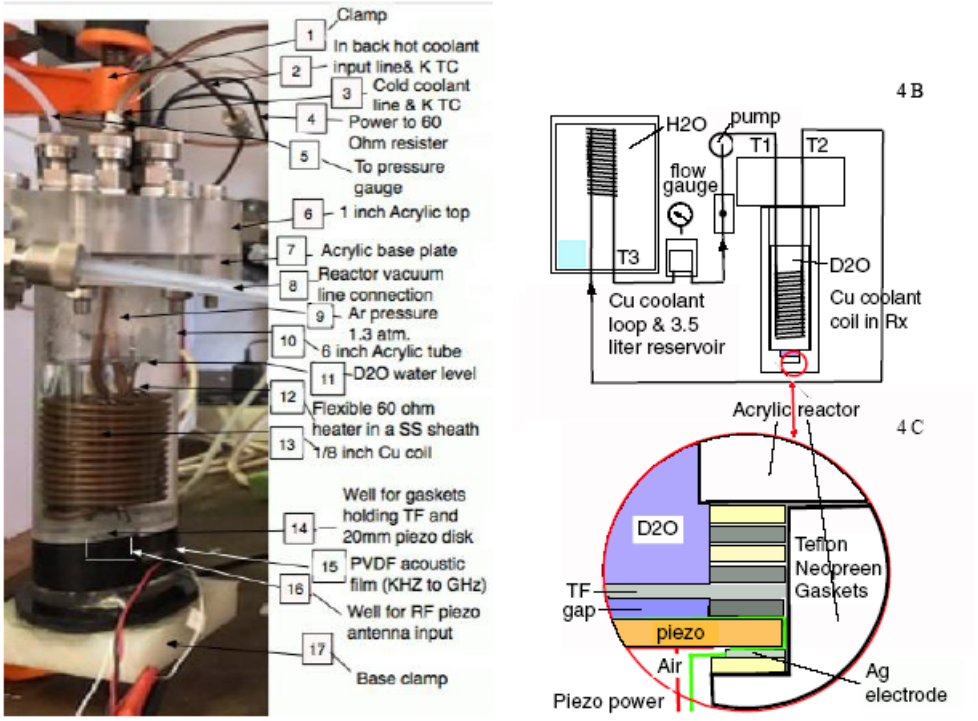

Figure 4. (A) The acrylic RF reactor is compressed to seal the Ar-saturated D_2O. The bolted top plate, 6, holds all the connections. The heat removal Cu coil is completely covered by 80 g of D_2O, Fig. 4B. The 60 Ω resistance heater from ARI was completely submerged, 11. The gas phase Ar, 9, with a trace of D_2O was present at its vapor pressure at a total pressure of 1.5 atm. The 20 mm piezo disk, RF piezo, is centered in the bottom with the target foil, approximately 1 mm above in the cavitating D_2O. (B) The coolant loop between the reactor and 3.5 l coolant reservoir maintains the steady state temperature during the power inputs to the RF and calibration modes. Note the flow control was by the FMI displacement volume pump at ∼1 ml/s. (C) The red circle shows a corner of the acrylic reactor in light blue; the placement and sealing of the TF, 5×18×0.01 mm^3, and piezo shows the 1 mm gap. Bubbles are formed in the gap and the top and bottom of the TF surface f_1 and f_2 surfaces of the target foil (see Fig. 2). The piezo ground Ag ring with green lead and the positive input is red bottom service for the 1.6 MHz PZT 20 mm disk piezo. The Teflon and Neoprene gaskets are spacers and seal for the piezo and TF.

removed to the 3.5-liter coolant water cooled by Cu coil #2. The sum of these two DTs is the total heat produced by the running reactor.

3.2. Experimental set-up

The RF system gathered data using a video camera correlating the many parameters, using the sweep second of the clock, #14, to point out and store any running changes during an experimental process. The geometry of the RF run from the 50-g polycarbonate circulating D_2O liquid system uses a 5 ×1.5-inch column of D_2O while keeping the static D_2O close to steady-state temperature by using a 16 loop Cu coil. The coil is 1/8-inch OD and about 2 inches long submerged in the D_2O. The setup required about 1000 s to reach steady state.

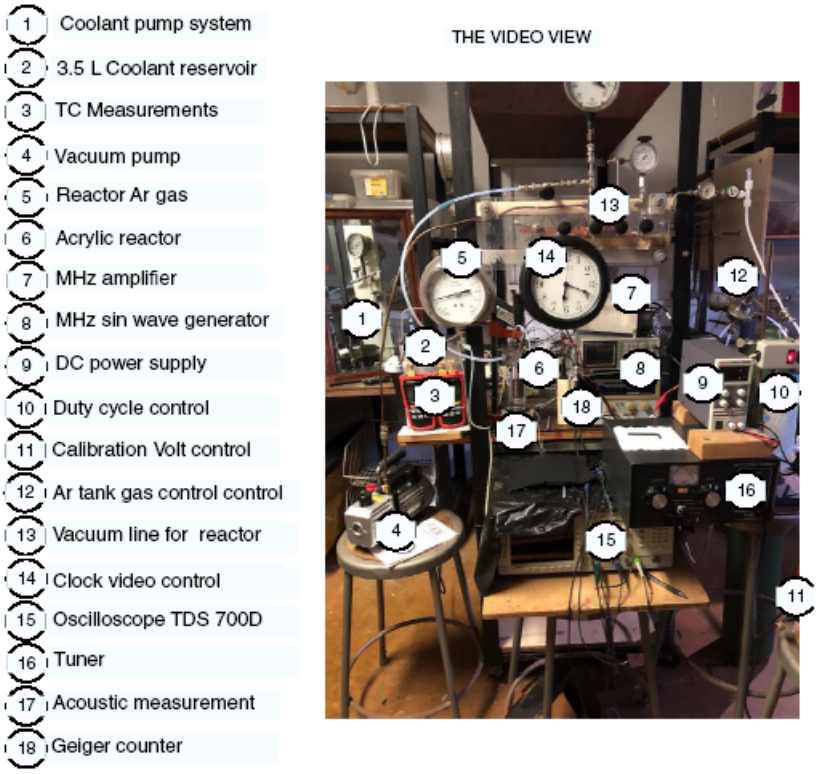

Figure 5. The video screen is set in the plane of the clock #14 to cover as many parameters as practical. The Cu coils #6 and #2 form a loop moving heat from #6 to #2 (see Fig. 4B). The coolant circulation that is exempt from the duty cycle flows at a measured rate of about 1 ml/s (#1). The RF input signal is provided by an Eventek 3010D audio-amplifier (#8). The HD communications HD30866 RF amplifier and its DC power supply are shown as items 7 and 9, respectively. The oscilloscope #15 and tuner #16 monitor the RF signals. The vacuum gas system involves the vacuum pump #4, vacuum line #13 and the Ar tank #12. PVDF sensor film #17 detects the complex beat signal in the MHz range indicating the presence of two signals with approximately equal RF intensity.

3.3. Example of collected data from RF run RF4 D_2O and Pd

Explanation of Fig. 6

Moving Reactor heat from the reactor to the 3500 ml water coolant reservoir reducing the running temperature. The heat measured via T2 - T1 90 (Cu oil in and out) for both run and cal. mode. The cal. mode substitutes a 60 Ω, 10 W heater input for the RF input. coolant water flow rate is measured is for the combination One and Two reactor inputs for the Cal. Mode. The total watts input comes from the resistance heater, $V_2/R = 202/606.7$ W. One, at measurer the output coolant flow 1.08 ± 0.02 ml/s. There is a continuous heat loss to the coolant keeping the running low as possible (good for the cavitation process). The power input from a 20 V Variac is 6.7 W. The key is the power loss to the 3.5 l coolant heat gained at a steady state temp of 3.2°C. The rate of heat loss operating at low DT. The total heat is 6.7 and provides a scaling factor for the run mode. The 6.7 W produces 3.2°C. For the RF input it has the same temperature drive for the same 87 g of D_2O. An Attempt was made to make the two modes and running during cal. modes. The 6.7 W input and temperature for the cal. mode is the scaling-factor for watt calculations: Run, Cal.

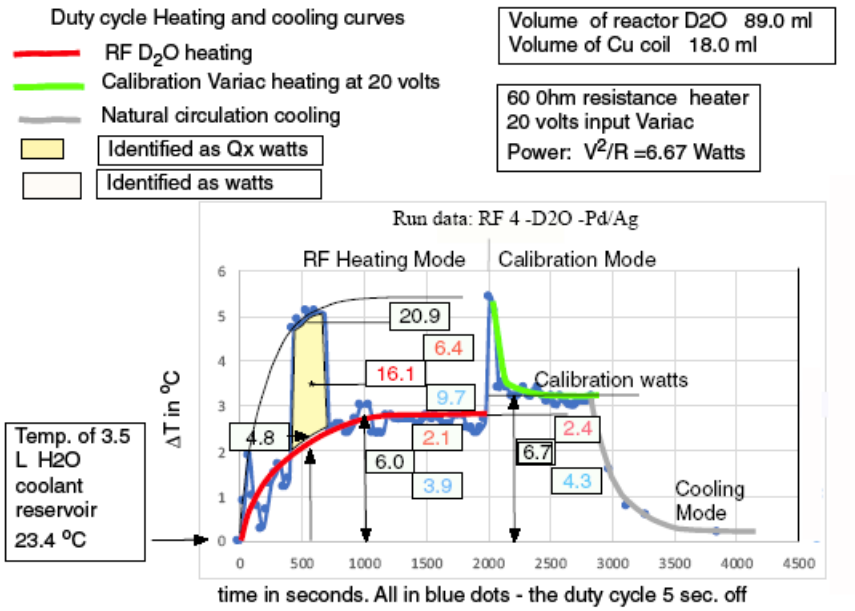

Figure 6. See the Explanation of Fig. 6 below Section 3.3

and Qx modes shown in Fig. 4. Run RF #4 D_2 and Ag. The RF data, blue dots, are are reduced to numbers, and are keyed to the calibration mode resistant heater Watts input. Volts$^2/\Omega$ = 6.7 W during the duty cycle. This value scales with temperature °C.

3.4. Typical RF mass spectral analysis

Run # RF 4 D_2O and Pd. Data collected Apr. 30, 2018 and shown below the MS RAS ^{4}He analysis by Malcolm Fowler, in Fig. 7. His MS measurement was 0.363 ppm in D_2O

3.5. RF EDX data

EDX of RF cavitation TF surface.

4. The Meso-cluster

4.1. A possible model

When trying to explain the RF process presented in Fig. 9 as a single event, one consideration is to think of the MC as a group of deuterons acting as a single unit in time frame A. The MC can be thought of as a small collection of charged bosons under compression at a high temperature. The deuteron density increased due to compression and due to the neutralization process ($D^+ + e \rightarrow D$) within the hot plasma of the MC. The instantaneous charge communication kept the neutralization process from occurring at the end of the neutralization drive of the plasma when the temperature dropped near the end of time line A. The point of a single recombination of the D atom produced a corresponding SW

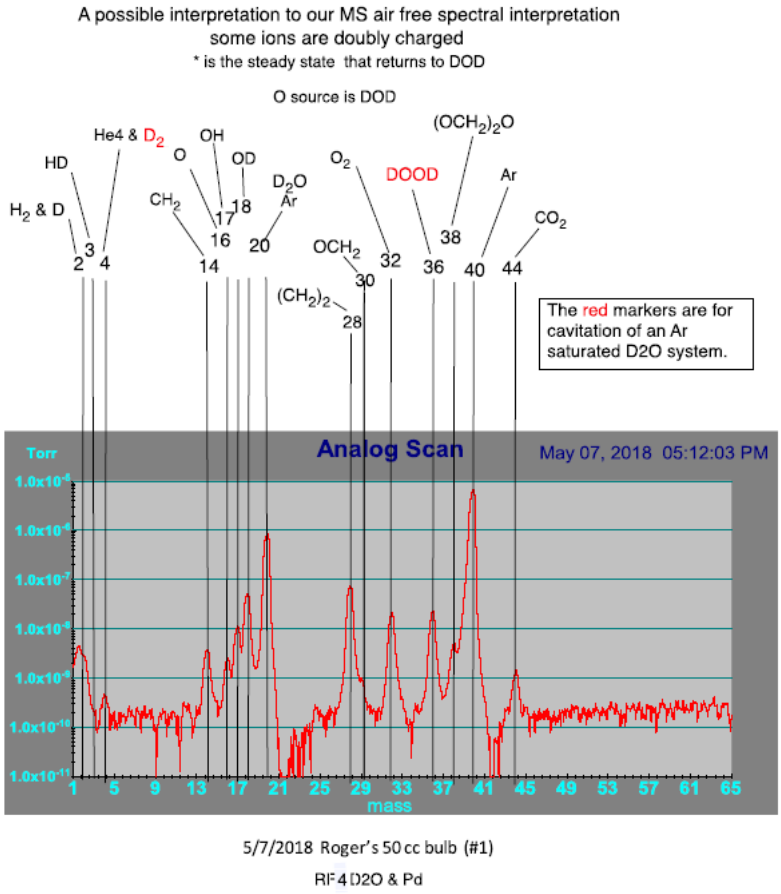

Figure 7. From [2] "Chemical species generated under ultrasound irradiation are attributed to the acoustic cavitation phenomenon". Under Ar bubbling, the species detected during the sonication of pure water are H_2 and H_2O_2 in agreement with the following equations transposed from H to D: $D_2O \rightarrow H + OD^{\circ}; D + D \rightarrow D_2; DO^{\circ} + {}^{\circ}OD \rightarrow D_2O$.

that stimulated alpha formation in the MC that had been neutralized with one cooled electron. One alpha was produced in time frame A, during the charge separation and neutralization process at the expense of one MC.

The above paragraph describes the timeline A shown in Fig. 9; the evolution of the MC is governed by the implantation of squeezed electrons and deuterons. Charged particles are driven toward charge neutrality in the MC plasma. The plasma remains below the critical density required to trigger the D atom shock wave (SW); this delay produces high compression temperatures due to the collapsed bubble cavitation jet resulting in squeezed and focused spherical compression of the deuterons forming the MC (Fig. 10B). The free mobile electrons implant first, followed by the less mobile deuterons to form the charged-separated MC plasma. Compression heating also occurs in the confining target foil lattice atoms by adding free ionized electrons that increase compression. The surface-implanted electrons are initially separated from the implanted deuterons in time frame A; the deuterons are electrostatically compressed in the squeezed MC plasma via its spherical piston action at the TF surface for ambient face-centered structure, and in the TF volume for ambient body-centered structure.

EDX of RF cavitation TF surface

		GRAPH 1	GRAPH 2	GRAPH 3
Atoms identified Num.	Type	H2O RF3 Pd	D2O RF4 Pd	Piezo RF 2 Pd
8	O	80.0	59.0	23.10
46	Pd	7.9	22.9	---
14	Si	4.9	15.3	9.14
13	Al	2.6	0.5	----
29	Cu	1.04	1.01	6.34
28	Ni	0.97	0.69	42.9
12	Mg	1.77	0.00	----
26	Fe	0.58	0.75	----
16	Su	0.11	0.61	----
40	Zr	0.00	0.40	----
15	P			0.71
22	Ti			3.55
6	C			2.97
11	Na			0.83
7	N			0.12
		~100%	~100%	~100%

Figure 8. Shows there were a lot of surface oxides, and the irradiated target foil surfaces showed the unique presence of the ^{24}Mg isotope in graph 1 of Fig. 8 from this series of EDX measurements. The reaction pathway to such a transmutation is obscure, but a pathway that utilizes ^{16}O, where 2O $\rightarrow ^{24}$Mg $+^{8}$B and ^{8}B $\rightarrow ^{4}$He + alpha + β^{+} ^{8}B has a half life of 770 ms [6]. The isotope ^{24}Mg is unique in the EDX graph 1 of Fig. 8 and ^{16}O at 80% concentration in a proposed pathway to account for its EDX presence in a cavitating Ar-saturated D_2O fluid with implantation of plasma jets into a Pd foil. Graph 3 of Fig. 8 shows there is no Mg contribution from the piezo. Both the D_2O and H_2O EDX graphs had target foils of Pd that were cut from the same 0.1 mm stock from Ithaca. The volatility of a Mn complex is coupled with 12 mass-ratio in RGS mass spectroscopy of RF 3 H_2O and Pd collected products.

The plasma temperature at ∼10,000 K allows for charge neutralization, but no recombination to D atoms [11]. The collection of 2–20 squeezed deuterons form the MC. At the lower frequency of 20 kHz the MC population will be larger [3]. Under these conditions, the deuterons have a radius of ∼1 fm. The early-stage compression diameter of the MC is on the order of 1000–100 fm. As the compression progresses, the mobile electrons move into the MC, neutralizing its plasma charge; however, the elevated temperature prevents recombination to form neutral deuterium atoms.

Statistically, near the end of the compression cycle, the density increases and temperature decreases; under those conditions, the probability for a D-atom recombination in the MC increases. A single D-atom formation expands 10^9 times in volume in a femtosecond, initiating a local SW impulse in the MC space. This rapid space expansion impulse in the MC produces one or more alphas, and no detectable radiation. The impulse time is very fast making for a powerful local energy density impulse, which destroys the MC, produces alphas, heat, voids and micro TF spheres in the target foil lattice [12]. A single alpha-producing event requires 3.83×10^{-12} J (24 MeV), and this energy release is consistent with the energy required to form the observed single event ejecta sites. Numerous examples of single-event ejecta sites are found in SEM photos of target foils with face centered cubic crystal structure. Target foils with body centered cubic crystal structure do not exhibit the single-event ejecta sites (unit crystal lattice).

Evidence of alphas was found in several target foils where surface alphas were ejected at the surface of the target foil and are associated with surface craters and micro-spheres, as documented using scanning electron microscope photography (single events). The presence of crater ejecta was always associated with ^{4}He in the collected gas samples of argon-saturated D_2O measurements. When the data was examined for surface craters in BCC Ti target foils, none

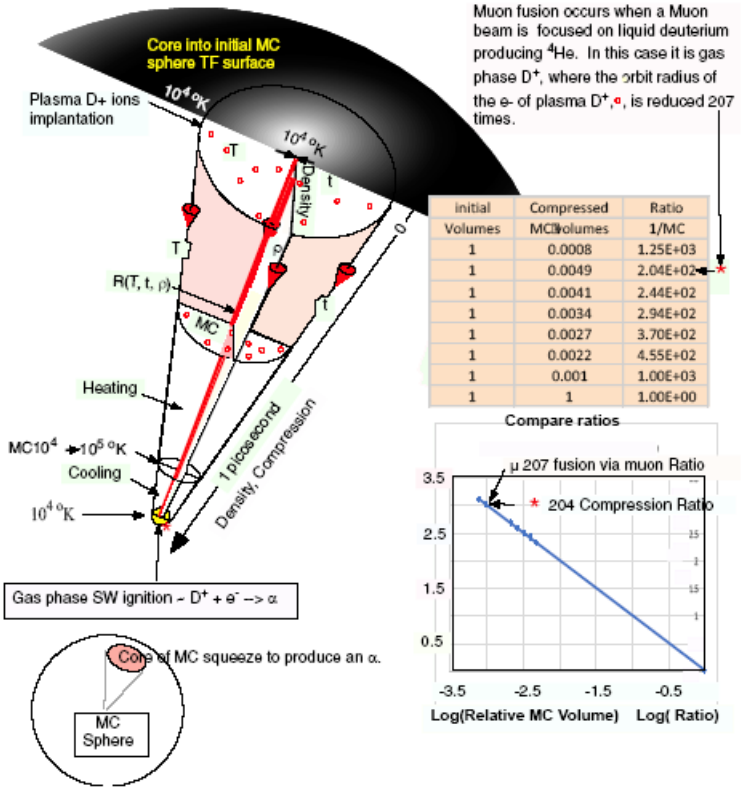

initial Volumes	Compressed MC Volumes	Ratio 1/MC
1	0.0008	1.25E+03
1	0.0049	2.04E+02
1	0.0041	2.44E+02
1	0.0034	2.94E+02
1	0.0027	3.70E+02
1	0.0022	4.55E+02
1	0.001	1.00E+03
1	1	1.00E+00

Figure 9. The figure shows the reaction sequence following the ($D^+ + e$) plasma implantation, comparing MC fusion to muon fusion [1]. The black sphere is the MC at T on the time line A. A core from the MC is visually expanded to reveal the stages during the time line A. Electromagnetic compression and the magnetic target foil containment of the MC contents initiate the pathway to ^{4}He production. Three important parameters, temperature, time, and density are aligned with the red core MC compression in the implanted TF lattice. Note in Fig. 9 that as time advances, the contents of the MC are brought closer together by compression; this action and the two graphs show the similarities to muon fusion, which in this case occurs at an effective temperature of 10,000 K. The compression of deuterons conjectured here occurs much faster than muon fusion [7] (see Fig. 3); the fusion conjectured here occurs at a much higher temperature using an SW in the MC plasma ($D^+ + e \rightarrow D$). The impulse energy is derived from the shockwave's destruction of the MC in the blue cooling zone with D atom recombination, producing an alpha event and ^{4}He (also see Fig. 13).

was observed. Mass spectrometry shows that ^{4}He is trapped in the active Ti TF lattice volume. This was concluded when $3.83 \times 10^{+12}$ ^{4}He atoms above measured background levels were released from a vaporized sample of Ti TF [1].

So, there is a dilemma. Reactive face centered cubic (FCC) target foils produce ^{4}He with numerous single-event ejection sites at the TF surface; by contrast, body centered cubic (BCC) target foils trap ^{4}He somewhere in the lattice. The evidence shows that alpha activity in the FCC target foil is expressed by alpha ejection at high temperature, while alpha activity in BCC target foils is trapped within the host metal. The FCC unit crystal has twice the number of atoms as the BCC. Why is there a difference between FCC and BCC target foil activity?

There have been fragile 1 μm diameter hollow tubes observed in SEM photos [8–10], and much evidence from other sources. These tubes are fragile and not expected to last more than a fraction of a second. There is a critical

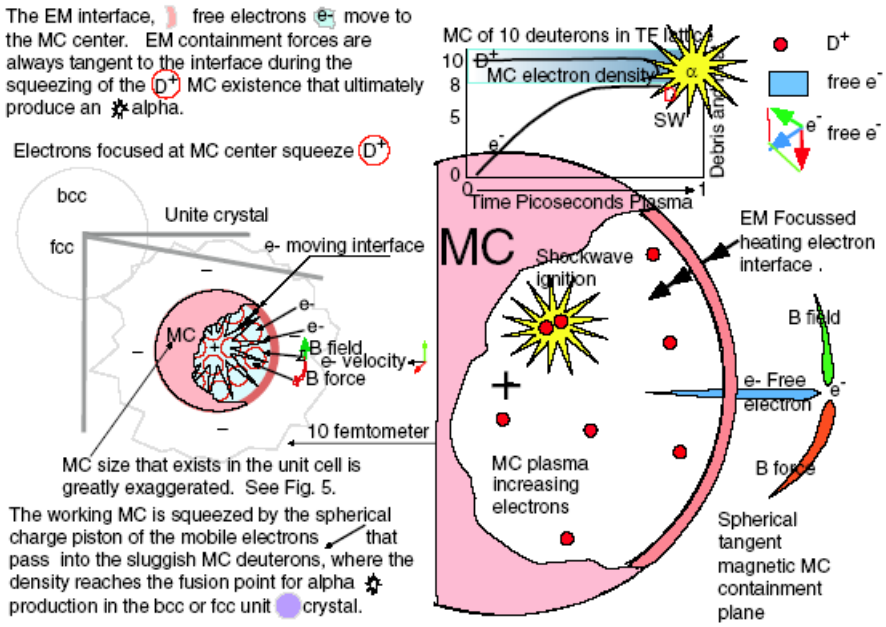

Figure 10a Figure 10b

Figure 10. (a) Shows the possible connection of the unit cell to the MC The gray lines indicate the placement of the MC in the unit cell in time frame A. The purple sphere is the corner of a BCC or FCC unit cell. Of the many different target foils tested, the only BCC lattice crystal measured was the hot surfaced titanium target foil. All titanium foils tested had TiO_2 microtube surface layers of iridescent color consistent with a surface standing wave. The measured titanium target foil, Ti-3A, produced ^{4}He that was located in the interior lattice structure of the titanium foil. By contrast, The FCC target foils showed a substantial number of single- event surface craters that are perhaps equivalent to the energy of one alpha event and will be treated that way in the text that follows (ICCF 20). Therefore, the ^{4}He measured from titanium target foils not showing ejecta sites was not consistent with two Palladium samples that showed many ejecta sites, but no lattice ^{4}He. (b) Shows the detail of the MC and its surrounding free electrons; the light blue sphere to the right is focused at the center of the MC sphere. The graph at the top shows the penetration of electrons that neutralize the plasma but are too hot to recombine [13]. The movement of electrons, by way of the electromagnetic force, compresses the MC contents. Momentum carries into the cooling mode of spherical charge as the electrons move to the center of the MC, where a D atom forms, creating an impulse SW capable of producing heat and ^{4}He.

difference between the BCC and FCC target foils, based on properties of the unit cell [13] or differences based on other factors yet to be considered.

4.2. Summary of the activity within the MC

Figures 10a and b depict the MC activity in time frame A (less than a picosecond) from the point of view of the MC itself. In the model, the MC is a cluster of deuterons that have an affinity and repulsion for each other, being hot bosons surrounded by mobile elections in a charged-separated plasma containing only deuterium ions [14]. The radius of a D^+ is just over a fermion and the electromagnetically compressed MC will locate somewhere interstitially in the unit crystal (see Figs. 10A and 11B). The unit cell for the FCC contains four atoms, the BCC unit cell contains two atoms and is one-half as large as the FCC unit cell. The MCs can locate anywhere in the host metal lattice. They are sufficiently small so that all components are only slightly larger than one fermion.

Figure 10a shows the corner of a unit cell and the MC dimension that shows a free electron pushing concentrically inward to a focus point while the mobile electron generates a magnetic field with force tangent to the interface. The electrons are the only particles moving in time frame A. Figure 10b depicts the conjecture that the deuterons contained in the MC can be compressed by forces that include the force of an orbiting electron. It is also conjectured that the chemical energy (15.5 eV) released during atom–electron recombination is sufficient to produce D+D $\rightarrow$ ^{4}He + 24 MeV because of the high particle density within the MC. The proposed ignition energy comes from $D^+ + e \rightarrow D +$ 15.5 eV, producing an effective high energy shock wave pulse that forces at least two deuterons in the MC to fuse.

4.3. The drive to neutrality

For discussion purposes, assume the MC contains 10 deuterium ions and no neutral deuterium atoms at a high temperature with electrons moving through the interface without recombination during the time frame A. The MC volume remains small, with its cluster of ten deuterons as an example. As the MC cools at the end of its compression cycle, a recombination occurs resulting in a shock wave with sufficient impulse energy to produce the $D^+ + e \rightarrow D + 15.5$ eV chemical reaction. The mobile electrons have a temperature, a velocity, and a direction that keeps the MC compressed and heated. It is proposed that the initial out of balance charge distribution drives the increasing energy density toward that of a muon fusion environment and is driven by a natural electromagnetic compression. At high temperature, Faraday's law of induction forces a mix of electrons and deuterons to form a neutral plasma, without forming neutral deuterium atoms [15]. The temperature is high and the impulse time (see Fig. 13), is of short duration, so there is no recombination forming neutral deuterium atoms (marked in red in Fig. 10b). At the end of the MC cooling cycle, an increase in the probability of recombination occurs, destroying the MC. A SW impulse of high energy density produces ^{4}He and heat. The electron energy, velocity, temperature, mobility, and time are in resonance to produce this single event (see Fig. 10b).

4.4. The cycling of MC and electron mobility

The TF crystal system in time frame A at high temperature was not mobile enough to alter the solid phase periodicity order. In time frame A, the unit cell structure of FCC and BCC location of atoms was still intact. Although there is a possible interchange of crystal structure FCC to BCC at an atomic level at 1200 K [13] the lattice phase does not change much. The MC should be considered as an interstitial addition to the target foil lattice (see Fig. 11b). Modification of the melted surface of the target foil will keep changing to a fine-grained surface lattice, with the grain boundaries taking up the debris, as it is cycled through a continuous heating and cooling process. This atomic scale cyclical process alters the surface of the target foil to an approximate depth of 100 μm; low frequency cavitation input produces more target foil damage than does high frequency cavitation input as evidenced by SEM photos [3]

The surface of the TF in a cavitation field is generally exposed to small energy pulses continuously heating and cooling several million atoms at any given time. Recrystallisation tries to follow the input frequency by decreasing the surface crystal size as the frequency increases. Cavitation bubbles decrease in size as the surface tension increases. As the energy of the system decreases, the energy density increases so smaller systems have a better chance at making alphas. The smaller implanting events of the MC containing only a few deuterium ions are at too high a temperature to react. When the deuteron temperature declines slightly, a deuterium ion and a single electron can recombine to produce a small but energy-dense shock wave and an alpha.

The electrons in a high temperature environment of non-recombining plasma of deuterons and free electrons are focused on the squeezed deuterons. These short-lived MC-implanted deuterons are further heated and squeezed by these moving electrons to produce a fusion event in time frame A. The plasma electrons are the only species with mobility and are focused on the MC-implanted deuterons. The MC system is driven by charge separation driven to

neutrality in a process similar to muon fusion. As the MC deuterons reach a density similar to that of muon fusion, alphas begin to appear in the lattice [7].

5. Discussion

5.1. The FCC and BCC differences

The unit cell of Ti contains two atoms with a coordination number 8, and FCC contains four atoms, with a coordination number of 12 for their cubical and reciprocal lattices. The coordination number is the number of atoms touching in the unit cell. The reciprocal lattice of the BCC is the actual lattice of the FCC and vice versa. The X-ray diffraction patterns of BCC crystals are the same as the actual FCC unit crystal atom lattice distribution. The symmetry lines from the center of Brillion zones and Wigner–Seitz unit cells define their symmetry points. The Brillion zone for FCC is BCC and the BCC is the FCC Brillion zone. The mobility of free electrons dominates the time frame A of the MC with gas-phase probability of zero for finding an electron orbital to form the D atom producing the SW (SW)of $2D^+ \rightarrow \alpha$.

The probability of finding an electron orbit in the MC is zero, and not until the temperature and density are favorable to recombination ($D^+ + e \rightarrow D$) will there be a recombination event to produce a SW impulse to create an alpha in the compressed MC.

In earlier experiments, ^{4}He was measured in the Ti bulk lattice either retained near the surface or deep in the lattice, as opposed to palladium target foils which produced ^{4}He in craters formed at the surface. It is more likely for helium to be near the surface of the target foil than in the bulk lattice. The titanium target foils had a TiO_2 surface layer and trapped ^{4}He in the Ti lattice. The palladium target foils were different and showed no measurable ^{4}He above background level in the metal but it was observed that ^{4}He was ejected from the palladium at sites that originated in the near surface. It was found that the energy required to remove the volume of ejecta observed in a single site was about 24 MeV, which is consistent with the energy released for the D+D $\rightarrow ^4He^+$ 24 MeV reaction. These crater sites are about 50 nm in diameter and depth. The number of palladium lattices in the ejecta volume is calculable and the energy to disrupt a single palladium lattice is known to be about 21 eV. So, the ejecta volume observed in a single crater suggested a single nuclear reaction of approximately 24 MeV. These small events were seen in low frequency events with more damage in high resolution SEM [3]. The SEM photos with high frequency experiments show the relationship between ejecta volume and single alpha production. Palladium lattice atoms that are ejected from craters along with alphas have been shown in many SEM photos. Various sized craters have been observed with ejecta volumes corresponding to an implied energy release in the form of integer multiples of 24 MeV single energy events. Measurement of ejecta volume is then conjectured to be an indirect measurement of the Q for the reaction that produces alphas in deuterated palladium. No gammas were found that could relate to one or more alpha events. These correlated ejecta events were observed for FCC crystal lattices of Pd, Ni, Cu, and Ag. This finding is in contrast to observations made in the titanium BCC crystal lattice. A titanium target foil sample was studied by Brian M. Oliver in 1994 that measured $40\times10^{+12}$ ^{4}He atoms, trapped in the exposed titanium, as analyzed by mass spectroscopy at Pacific Northwest Laboratories. There was no evidence of ejecta damage revealed by the several SEM photos taken of the sample surface.

The jet plasma surface implantation into the titanium target foil where the titanium BCC surface is modified by the presence of TiO_2 may explain the difference between FCC and BCC with regard to crater formation. The titanium sample surfaces contain deep layers of multi-colored iridescent standing wave patterns of TiO_2, featuring micron diameter tubes [8]. These surface differences may explain why the FCC target foils produce alphas at the surface while the BCC target foils produce alphas in the metal volume. The deep layers of TiO_2 buildup on titanium target foils by D_2O cavitation may influence the location of alpha production.

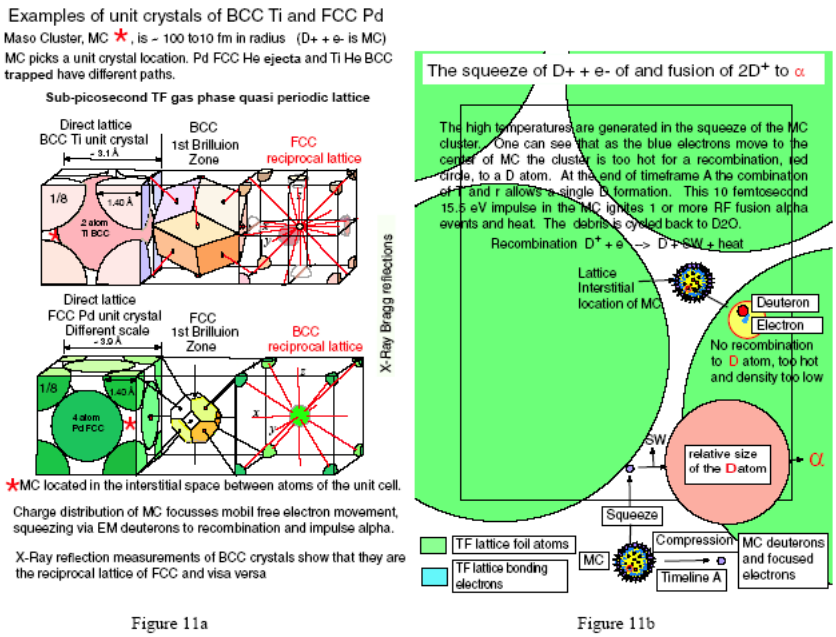

Figure 11a Figure 11b

Figure 11. (a) Shows the periodicity of the TF lattice that for a sub-picosecond is stationary except for the mobile high temperature free electrons on the MC in the titanium BCC lattice or palladium FCC lattice. The compressed MC of deuterons is located in the interstitial space between atoms of the target foil. The red stars shown in (a) depict the spherical free electrons that compress the MC. The presence of many free electrons raises the temperature of the atoms contained in the TF lattice. Note that the unit cell of the BCC is the reciprocal lattice for the FCC lattice and vice versa, so the containment void space may have some important differences.

5.2. Unit crystals and MC deuterons

Figure 11b Shows that when the temperature remains high in the TF, the probability of filling any deuteron potential orbits in the MC is zero. Near the end of time frame A, the temperature declines and a free electron fills a single empty electron shell in the MC, releasing 15.5 eV of recombination energy. The deuterium ion rapidly increases in volume by eight orders of magnitude (8×10^{-38} – 8×10^{-30} m^3). The increase in volume occurs in 10 fs. A slight delay for cooling of the MC environment permits deuterium ion and electron recombination, forming an SW impulse of high energy density. Figure 13 shows an advantage the MC system has over the muon fusion system, using the 15.5 eV impulse SW within the compressed MC space. This SW fuses two deuterium ions into a single alpha, with heat dissipation in the target foil lattice and surrounding D_2O at the MHz frequencies. As the frequency is reduced more multi-ejecta events are observed [3].

5.3. Muon fusion and RF cavitation fusion

The energy density ratios are 10^9 higher for the deuterons in the MC than the $t\mu + D_2$ reported in muon experiments [20]. The energetic deuterium ions in the MC, with no jet plasma electrons, mix with neutralizing electrons during time frame A to produce a single D atom SW and an alpha. The muon requires more time and energy to substitute a μ for an electron to produce a large molecular ion decaying to an alpha. Muon experiments use the volume of the combination of $t\mu + D_2$ to produce a ^{4}He atom with its orbital electrons. Muon based systems require 10^{-7} s to

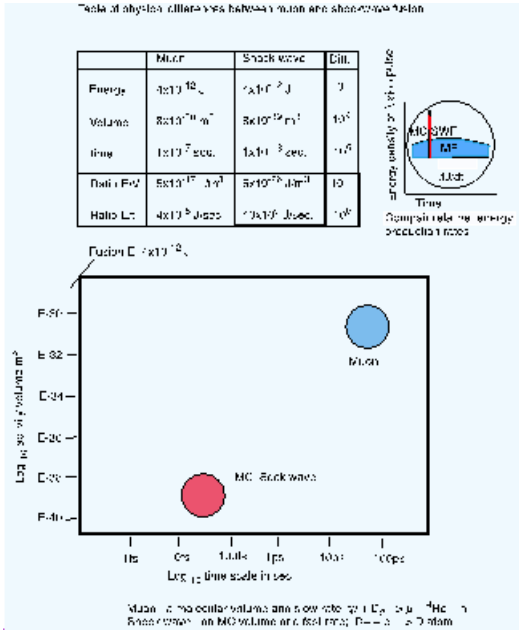

Figure 12. Shows a rough comparison of the energy, density, and time scales in a muon fusion event and an MC fusion event. It can be seen that MC events occur in a much smaller volume, and a much shorter time window. The diagram in the upper right of Fig. 12 shows that a high-density energy pulse is associated with MC events, which is conjectured to promote D–D fusion [16–19]. Note the time line spread of the muon fusion pulse event compared to the SW pulse event.

produce a single ^{4}He compared to 10^{-13} s for the alpha produced by SW fusion.

5.4. Photon emission and coupled acoustic pick-up

The SL emissions were measured by various multi pixel devices from a Hamamatsu MPPC 50, 100, and 1600-pixel resolution in a dark box. The average response to SL emission measurements was about 0.05 V shown as blue peaks in Fig. 3. At 1.7 MHz of piezo input, there is a 100 ns SL photon emission cycle (blue peak in Fig. 3) and 1.6×10^6 photon emissions per cycle calculated from this data that are coupled to the piezo frequency. The same coupled frequency is also found in the PVDF sound detection system showing a beat frequency of a second near-by frequency produced in the target foil (see Fig. 2). The SL measurements were made in a dark box minimizing the background light and cooled by the circulating water passing through the 0.63 MHz piezo device. These systems produced more than a million jet plasma sources per second. In these experiments, a Pd wire 0.0031 in. in diameter was used instead of a target foil with the cylindrical cavitation forces focused along the length of the wire. The piezo device had a 9 mm radius and 17 mm length with an ID of 4 mm.

5.5. Meso-cluster of deuterons

Free and highly mobile electrons are implanted in the MC and are influenced by attractive and electromagnetic forces; the electrons compress the MC and the deuterons contained within. At the end of the compression cycle, the MC temperature declines and the probability of recombination in the MC increases. An electron combining to form a neutral D atom produces the SW event. The SW is a high-energy impulse capable of triggering D–D fusion events.

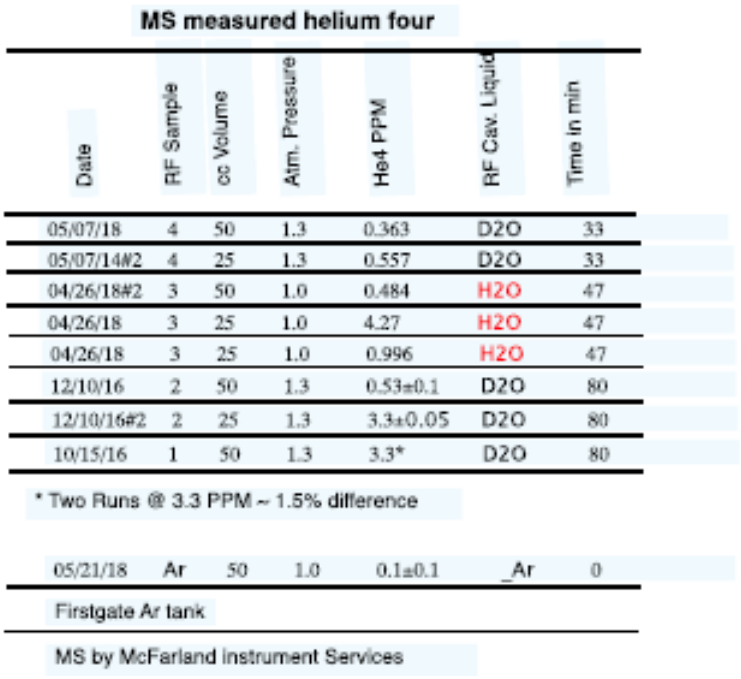

MS measured helium four

Date	RF Sample	cc Volume	Atm. Pressure	He4 PPM	RF Cav. Liquid	Time in min
05/07/18	4	50	1.3	0.363	D2O	33
05/07/14#2	4	25	1.3	0.557	D2O	33
04/26/18#2	3	50	1.0	0.484	H2O	47
04/26/18	3	25	1.0	4.27	H2O	47
04/26/18	3	25	1.0	0.996	H2O	47
12/10/16	2	50	1.3	0.53±0.1	D2O	80
12/10/16#2	2	25	1.3	3.3±0.05	D2O	80
10/15/16	1	50	1.3	3.3*	D2O	80

* Two Runs @ 3.3 PPM ~ 1.5% difference

05/21/18	Ar	50	1.0	0.1±0.1	_Ar	0

Firstgate Ar tank

MS by McFarland Instrument Services

Figure 13. Values for the mass spectrometry results for the RF reactor system are tentative; Results from a new mass spectrometer are discussed in a parallel ICCF 21 paper by Tom Claytor, Malcolm Fowler, and Roger S. Stringham.

In summary, the MC is compressed to fusion by reducing the distance between D ions so alpha fusion occurs as in muon fusion. At high cavitation frequencies, there are single or multi fusion events in the target foil and release 3.83×10^{-12} J (24 MeV) of energy per D–D fusion event. The MC is destroyed in this process and its remnants have been detected by mass spectrometry and SEM; they were found to be similar at all applied frequencies and have similar concentration levels [3] reverting back to the D_2O, and the steady state D_2 and DOOD. The RF cavitation process, with its alpha output, requires about 10^{13} fusion events per second from a one cm^2 target foil to produce 40 W of anomalous power. Note that the MC event at low frequency, 20 kHz, systems are dominated by large destructive multi events and with some single MC events (basic minimum event is the formation of one alpha). The MHz frequencies are typically single events with a few 2 and 3 FCC ejecta crater events.

5.6. Table of MS ^{4}He measurements

Mass spectrum measurements by Malcolm Fowler of MIS labs in New Mexico of RF samples delivered from Firstgate Energies lab in Hawaii.

5.7. Structural coloration

Thin oxide colored films are formed on the target foil surface. Ordinary sunlight striking the surface of a target foil that has been exposed to D_2O cavitation may have a high degree of coloration and patterns that are controlled by the input power and frequency of the D_2O cavitation. It is conjectured that the coloration is a result of standing surface waves;

such standing waves are influenced by target foil edge binding during cavitation in the reactor. The TF thickness (generally 100 μm) is exposed to surface oxidation and the high temperatures influence the color showing standing wave patterns on the TF. The colorations are particularly strong for the BCC titanium target foils. These target foils have no ejecta craters but the exposed surface was highly colored. Run # 17 tested in 1995 consisted of a 5 cm^2 and 100 μm thick foil of titanium. The sample was placed in a 46 kHz cavitating D_2O reactor and secured at four corners of the foil. The exposed foil's surface was colored by an iridescent pattern of a standing wave that covered about 1/3 of the exposed foil. The pattern was geometric repeating and showed a 2-dimensional multi-color square pattern about 3 mm on a side. A zirconium foil showed the same pattern. Ti and Zr are both body-centered cubic metals (BCC). The other three target foils in this sample group were face centered cubic metals (FCC) and showed surface ejecta sites at all frequencies tested. The smallest ejecta site was $\sim$50 nm in diameter and 50 nm deep, and required about 4×10^{-12} J (24 MeV) of energy to form the crater.

From surveys of many SEM photos, FCC target foils showed ejecta damage, but BCC target foils did not. Ti and Zr are BCC metals. There is evidence in the BCC target foils for a multi-layered TiO_2 surface build-up and small micron-diameter tubes [8,9]. In cavitation systems, the same tubes are produced but are so delicate they fragment in the cavitation field [12]. The exotic coloration in structured layers found in exposed titanium target foils may derive from the same physics as that which explains the coloration found in oil slicks and bird feathers [21]. The strong coloration is the result of TiO_2 thickness on the titanium target foils and shows the 2-dimensional surface pattern in color variation that relates to a build-up of TiO_2 via the resonant frequency of the acoustically driven target foil [12]. The surface of BCC titanium is made up layers of titanium oxide, anatase, rutile, and brookite as a mixture. The standing wave alters the thickness of the oxide layers.

5.8. Temperature of events

Target foils of a thickness of about 100 μm, were placed into a cavitating reactor, and depending on the frequency applied to the exterior surfaces, the target foils immediately lost their original surface appearance. This is typical for the start of any cavitation run. When the cavitation operates in the MHz range, the surface crystal structure is melted, cooled and cycled more than a million times per second in the MHz range. At 20 kHz it is possible to observe the surface while running and observe a glistening that will disintegrate the target foil if the power input is too great. This phenomenon is altered by increasing the frequency [3]. This altered target foil surface structure typically changes to a very fine-grained surface in the target foil's active area. During reactor operation, the target foils are slowly changing by forming surface oxides and fine-grained surfaces, where events start at the beginning of the run and continue with the slow destruction of the target foil surface.

Face centered cubic (FCC) target foils continue to lose mass through ejecta sites from the surface of the FCC foil. The bulk of the target foil system is at a steady-state temperature; an isolated event that produces the fusing SW that is in the range of 10,000 K has little effect on the bulk steady-state temperature. Events are made up of about 2–100 charged particles in the MC and are a one-time TF surface event that produces alphas in a self-destructive process. During the particle plasma compression cycle, ejecta craters are formed, and are about 50 nm deep with a 25 nm radius. Measurements from SEM photos and mass spectrometer measurements show alphas only exist near the surface of the target foil. The above statements hold true for the FCC target foils but not for BCC target foils. Titanium target foils produce ^{4}He, as detected by mass spectrometry but the ^{4}He is found in the bulk and ejecta sites are not observed [1]. At the elevated temperatures produced by high-frequency cavitation, deuterium exists mainly in ionic form. The cavitation process provides continuous rebuilding and recycling of the older target foil surface, maintaining a fresh active surface area on the target foil for D–D reactions.

The palladium TF surface is initially very bright and smooth but after 5 min of cavitation a hole in the surface is often produced at 20 kHz in high-power mode. There are archived videos of this process. When testing palladium

target foils, new surfaces are created and maintain the crater population at steady state, the new destroying the old, while altering the surface of the target foil with each cycle. This process creates a new recrystallized microstructure surface.

The titanium TF surface provides no barrier to the formation of MCs. The TF lattice provides containment of the MC, where the free electrons move toward the deuteron charge center. The MC plasma can be composed of say 10 deuterium ions and N concentric electrons; the MC deuteron sphere in time frame A is driven to charge neutralization.

Charge neutralization powers the compression of the spherical MC. The titanium TF (BCC) shows no surface craters or corresponding ejecta. It does show the same D_2O fragmentation in mass spectrometer measurements of D_2 and DOOD [2]. The titanium target foils are observed to have a gray paste adhering to the TiO_2 foil surface. The gray paste may be associated with the presence of alpha products, ^{4}He, and heat; the heat was dispersed through the 100-μm thick TF, cooled by the circulating D_2O.

It is the free electron mobility in time frame A when the ideal conditions in the MC are passed through that produces one neutral D atom, the 15.5 eV shockwave, a fusion impulse, and one alpha. During cavitation, this process can produce 10^{13} reactions per second, generating measurable and useful heat. This is the MC.

6. Conclusion and Summary

A good place to start is a paper that appeared in 1986 by A. Henglein Sonochemistry review, ultrasonic Vol. 25, 1987. His MS analysis confirmed the presence of the two markers D_2 and DOOD following D_2O cavitation; these markers were present from the very beginning of the measurements made in this 1986 mass spectrometry system. The markers were measured using mass spectrometer analysis of RF cavitation in Ar-saturated D_2O and were collected in gas samples that revealed their measured masses of 4 and 20 [2]. The markers in the Ar -saturated D_2O were in a steady state concentration.

The newer RF technology showed that at $\sim$2 MHz, ^{4}He was produced in 20 and 80 min experiments, without a good correlation of the produced heat as shown in Fig. 6. The emphasis was on the measurements for ^{4}He but the measurements do show a general correlation with evolved heat.

The RF technology is new but 2 years of work with Ar-saturated H_2O systems and solving RF interference problems preceded the experiments using D_2O. An RF duty cycle for reactor operation during both the active and calibration experiments was developed; measurements were made with the RF in off-mode to eliminate RF interference. The RF duty cycle was 30 s on, 5 s off. During the 5 s off period, reliable ΔT measurements were made. The duty-cycle method was adopted to make temperature measurements possible in the active RF reactor.

The advantage of the RF system was that you can use the 50-watt audio amplifier for a wide range of tunable frequencies at high amplitudes. The system was tuned by adjusting parameters to minimize the SWR, keeping it below 1.20. The reflected RF wave input should be minimized.

Samples of cavitation products were collected at the end of each run with vacuum transfer of 50 and 25 ml sample bulbs and were sent to the laboratories of Tom Claytor and Malcolm Fowler near LANL in NM. Experiment RF four D_2O and Pd was conducted on April 19, 2018; samples were taken and analyzed for tritium and ^{4}He. Figures 6 and 7 show the details of a typical analysis. The MS analysis, as mentioned in Fig. 7, showed the expected markers for the Ar-saturated D_2O cavitation and had a presence at all cavitation frequencies that were used. These RF systems heated water to steady state after about 1000 s with the heat exchange system in place (Fig. 4b). Heat was removed until heat-in equaled heat-out. Heat-in and heat-out were in balance via the two Cu coils. One coil was in the D_2O and the other coil was in the 3.5-liter H_2O reservoir, an isolated cooling system. The reactor temperature was kept at steady-state temperature (Fig. 4b). The acrylic reactor, while running, lost surface mass at the cavitating D_2O-acrylic interface; acrylic fragments were identified by the MS analysis (see MS graph Fig. 7).

One system that was run in a dark box and used Hamamatsu MPPC devices focused on the SL emission mea-

surements. In these runs at approximately 1 MHz of acoustic input, the active period was about 100 ns and the MC population pulse was spread over the active period during one acoustic cycle of 1.7 MHz. The rest of the time the system was inactive (see Fig. 3). This information can be used to estimate a maximum frequency for the bubble collapse mechanism.

In two cases, the ^{4}He measurements revealed either a concept failure or a ^{4}He removal failure. Two runs (RF 3 H_2O and Pd and RF 4 D_2O and Pd) measured ^{4}He, as shown in Fig. 13; measurements showed ^{4}He in light water and heavy water samples. These amounts were less than the ^{4}He concentration in atmospheric air. The saturated Ar-D_2O systems used Argon from a tank that was measured at 0.02 ppm of ^{4}He.

At the start of the experiment using light water (H_2O), distilled water was added to the RF reactor and was vacuum-pumped to remove all air bubbles from the RF reactor; this was the exact protocol used in the heavy water (D_2O) experiments. The only bubbles visible at the end of the pumping sequence were large H_2O vapor bubbles. At this point, argon was added to 1 atm. and the experiment proceeded along the normal path. The samples were collected and delivered to Claytor and Fowler. The mass spectrometry in this case was not as impressive as the ^{4}He measurements made by Brian Oliver of PNNP [1]. The light-water based RF Sonofusion samples showed as much or more ^{4}He than the heavy-water based RF experiments.

A comparison was made between the muon catalyzed fusion rate producing ^{4}He in its fusion process of μ capture or catalysis [7] to the RF, the mechanism rate that produces the SW that fuses two deuterons producing an alpha. The relative rates of RF and μ catalyzed fusion show that the RF fusion rate is millions of times faster and should be more successful (see Fig. 12). I am sure mass spectrometer measurements will improve and advance the cavitation know-how for control of alpha production and show if this is a fruitful path to a future that controls ^{4}He output and heat capture.

References

[1] R. Stringham, Helium measurements from target foils, LANL and PNNL, 1994, *J. Condensed Matter Nucl. Sci.* **24** (2017) 284–295.

[2] R. Pflieger, T. Chave, M. Virot and S.I. Nikitenko, Activating molecules, ions, and solid particles with acoustic cavitation, *J. Vis Exp.* **86** (2014) 51237.

[3] R.S. Stringham When bubble cavitation becomes sonofusion, *J. Condensed Matter Nucl. Sci.* **6** (2012) 1–12.

[4] URL retrieved from <http://nct resource center, FCC and BCC crystallography of metals>, 2018.

[5] P.A. Mante, M. Anttu, W. Zang, J. Wallentin, IJ. Chen, S. Lehmann, M. Heurlin, M.T. Borgstorm, M.E. Pistol and A. Yartsev, Confinement effects on Brillouin scattering in semiconductor nanowire phonic crystal, Department of Chemical Physics and Lund University, Swenden, APS.

[6] Isotopic data for boron and its isotopes is found in the Periodic Table.

[7] K. Nagamine, *Introductory Muon Science*, Cambridge University Press, Cambridge, 2003.

[8] C.M. Wen, N. Uekawa, K. Khamfoo and T. Kjimao, Titanium oxide thin film preparation with sol coatings of plate and spindle-shaped nanoparticles for control of optical transmittance, *J. Ceramic Soc. Japan* **124** (1) 60–65.

[9] N.J.R. Zhang, Y. Chen, H. Wu, W. Chen, C. Zhao and X. Zhang (2016), Study of cell behaviors on anodized TiO_2 nanotube arrays with different structures, FBIOE.2016.01.01130, Mar. 2016.

[10] V.V. Zheleznov, E.I. Voit, Y.V. Sushkov, S..A Sarin, V.G. Kuryavyi, D.P. Opra, S.V. Gnedenkov, S..L Sinebryukhov and A.A. Sokolov and A.A. Sokolov, Nanostructured microtubes based on TiO_2 doped by Zr and Hf oxides with the anatase structure, *IOP Conf. Ser.: Mater. Sci. Eng*., 11201, 2016.

[11] P.J.E. Peebles, Recombination of the primeval plasma, *Astrophy. J.* **153** (1968) 1.

[12] R.S. Stringham, Sonofusion produces tritium that decays to helium three, *Proc ICCF 15*, V. Violante and F. Sarto (Eds.), Oct. 5–9, 2009, p. 57, Some parts need a rewrite.

[13] Changing with increasing Tα phase of Ti is dominant and BCC changing from the β phase HPC, BCC and BCC.

[14] Julius Su and A William, Goddard III (advisor), An electron force field for simulating large scale excited electron dynamics,

Caltech, Thesis, 2008.
[15] R.S. Stringham, Conservation of E and M, single cavitation heat events *J. Condensed Matter Nucl. Sci.* **15** (2015) 55.
[16] K. Nagamine, *Introductory Muon Science*, Cambridge University Press, Cambridge, 2003, p. 79.
[17] Phillip Ball, We choose to go to the muon, Chemistry World, 2014.
[18] C.R. Nave, HyperPhysics, Muon Experiment, 2014.
[19] C.R. Nave, HyperPhysics, Atmospheric Muons, 2014.
[20] K. Nagamine, *Introductory Muon Science*, Cambridge University Press, Cambridge, 2003, p. 71.
[21] A.R. Parker and N. Martini, Structural color in animals – simple to complex optics, *Optics Laser Technol* **38** (4–6) (2006) 19.